1999 Review of the HCF/LCF Interaction Project in the PRDA V HCF Materials and Life Methods Program

Mr. Bob deLaneuville*[1],
Dr. Ken Bain[2],
Dr. Richard Bellows[3],
Dr. David Davidson[4],
Dr. Douglas Herrman[5],
Dr. Craig McClung[4],
Mr. Jerry Sheldon[1],
Dr. Bob VanStone[2],

[1]Pratt & Whitney, PO Box 109600, West Palm Bch. FL 33410-9600
[2]General Electric Aircraft Engines, One Neuman Way, Evendale, OH 45215-6301
[3]Allied Signal Engines, PO Box 52181, Phoenix AZ, 85072-2181
[4]Southwest Research Institute, PO Drawer 28510, San Antonio, TX 78228-0510
[5]Allison Advanced Development Co, PO Box 420, Indianapolis, IN 46206-0420

The US Air Force Research Laboratory PRDA V HCF Materials and Life Methods program, Contract F33615-96-C-5269, is a two + year industry program chartered with the development of High Cycle Fatigue(HCF) damage tolerant based methodology for the mitigation of HCF failures in turbine engine Titanium fan and compressor components. The HCF/LCF Interaction project is responsible for developing the data and models necessary to conduct HCF basic design analyses dealing with the influences of external loading conditions, of residual stress states, and of structural geometry (notches and stress gradients).

Program Organization

The program is administered by the University of Dayton Research Institute (UDRI) with Dr. Joseph Gallagher as the program manager. UDRI acts as program director, liaison between subcontractors, participant, technical advisor, and monitors the activities of the program's five major participants: Pratt & Whitney(P&W); General Electric Aircraft Engines (GEAE); Allied-Signal Engines(ASE); Allison Advanced Development Company(AADC); and Southwest Research Institute (SwRI).

Objective of the Program

The program will develop the methodology for a future Titanium fan and compressor components HCF design system, including FOD and Fretting. The program is divided into three projects, which are responsible for the primary damage states: HCF/LCF Interaction, Fretting, and FOD. The HCF/LCF Interaction project will focus on the interactions of HCF with low cycle fatigue(LCF) using Ti-6Al-4V as the model material. It will provide the core methodology to predict HCF capabilities from smooth and notch locations and will provide the basic methodology for the FOD and Fretting projects to predict HCF capabilities from those damage states, see Figure 1.

Problem Understanding

A review of HCF critical locations on an engine fan blade provides a good example of the complexity of the competing failure modes, see Figure 2. An understanding of the potential load cycling at representative HCF critical locations in a blade, the variety and complexity of the stress-time and stress-strain histories can be estimated.

Project Strategy

The strategy for the HCF/LCF Interaction project to develop the HCF design methodology is shown in Figure 3. The process is laid out such that the major task groups are cognizant of their responsibilities for both developing and exchanging the information necessary to accomplishing the goals and objectives of the program. The methods developed will be incorporated into a modular computer codes and implemented into life prediction codes for verification.

Test Matrix and Philosophy

The goal is to develop the basis for future design systems through characterization of Ti-6Al-4V to understand the interaction of HCF with LCF. The HCF/LCF Project will include specimen testing to satisfy material characterization requirements for the FOD and Fretting damage state projects. A condensed test matrix is shown in table 2. The more detailed description of the test matrices for this project requires six page of space and cannot be shown within the confines of this document. The goal of these tests are to determine material capabilities and damage states including the effects of potential dependent parameters such as frequency(10cpm, 60Hz, 1000Hz & 1600Hz), stress ratio(-1., 0.1, 0.5, & 0.8), and surface finish(baseline, peened, and various machined surfaces).

Test Results

A large majority of the specimen testing is complete and the following is a brief summary of the status and test results so far. Refer to Table 2 for list publications that contain more detailed results.

Test Methods Study

- Smooth fatigue specimen tests
  - ◊ Round-robin tests verified consistent test capabilities(P&W, GEAE, ASE)
  - ◊ Step vs extrapolated S-N test results are comparable for positive R-ratios=0.1, 0.5 & 0.8(ASE)
  - ◊ Negative R-ratio(-1.0) tests showed higher scatter and step test results are near-to or higher than extrapolated values(ASE)
- Threshold crack-growth tests(P&W, GEAE)
  - ◊ Shed rates as high as -20in-1 still gave accurate • Kth measurements(P&W, GEAE)
  - ◊ Analytical verification of high gradient accuracy(SWRI)
  - ◊ CT and Surface flaw specimen(t= 0.100" & 0.250") test results agreed(P&W, GEAE)

HCF/LCF Fatigue Characterization

- Smooth specimen tests
  - ◊ Goodman Diagram(R-ratio behavior) characterized(ASE)
  - ◊ Smooth specimen surface effects testing in progress(ASE)
  - ◊ Cyclic s-e/LCF tests complete(P&W)
  - ◊ Smooth Goodman extrapolation 107 vs 109 cycles, tests(P&W almost finished, GEAE begun Nov.)
- Notched specimen tests
  - ◊ Goodman Diagram(R-ratio behavior) characterized(P&W)
  - ◊ Variation of notch geometry and gage volumes suggests no effect on endurance limit(P&W)
  - ◊ Fatigue notch factors Kf & q established for Kt =2.5 at R= -1,0.1, 0.5 & 0.8(P&W)
  - ◊ Step vs extrapolated S-N tests are comparable for positive R-ratios = 0.1, 0.5 & 0.8(P&W)
  - ◊ Negative R-ratio(-1.0) tests showed higher scatter and step test results are near-to or higher than extrapolated values(P&W)
  - ◊ Peened notch specimens almost complete (P&W)
  - ◊ Deep notch effects testing started(SWRI)
  - ◊ Notched HCF/LCF mission tests, begun Nov.(P&W, GEAE)
  - ◊ Crack growth specimen tests

◊ • Kth Testing characterized for R-ratio behavior(P&W, GEAE)
◊ Long crack tests characterized da/dN for R-ratio behavior(P&W)
◊ Performed HCF/LCF interaction experiments in SEM(SWRI)
◊ HCF/LCF testing started (P&W, GEAE)
◊ Small crack testing not started(SWRI)

- *Multiaxial Fatigue Test Program - University of Illinois*

This program has just started(1/99) and its primary objective program is to run a limited number(~20) of tension-torsion fatigue tests to check available multiaxial life parameters. There will be a focus of multiaxial testing toward stress states that are representative of dovetail edge of contact areas. Testing will not answer all multiaxial questions, but will evaluate stress states relevant to the disk edge of contact

Materials Understanding

The focus of materials understanding for HCF/LCF interaction will be to characterize crack initiation mechanisms and crack growth modes. Distinguishing damage accumulation and crack initiation mechanisms is critical to appropriate modeling of dependent stresses and strains, for a given set of operating conditions (stress, strain-range, stress ratio, mission sequencing, specimen geometry and frequency). Smooth and notched HCF specimens will be analyzed using scanning electron microscopy to determine the mode of crack initiation (stage I or stage II).

Design Life Methods

The goal is to develop methodologies to predict fatigue crack initiation and propagation capabilities under combined HCF and LCF cycles. These fall into two categories, fatigue and fracture mechanics methods and the following lists show methods identified by team members for evaluation.

Total Life (Initiation)

1. Goodman Diagram
2. Multiaxial /Mean Stress Parameters
3. Local Stress-Strain models
4. Notch sensitivity methods
5. Notch plasticity models
6. Equivalent Stress /Strain Models
7. Initiation (Stage 1 and II)
8. HCF/LCF Damage Accumulation

Crack Growth

1. Small crack models (SwRI)
2. Shot peening models
3. Non-propagating cracks
4. Retardation (OP/UP)
5. Crack closure

Some of the approaches to accomplish the methods development are illustrated in figures 4, 5, 6, & 7. Methods development and evaluation is just getting started; there are no results to report at this time.

Methods Verification

A verification of these methods will be accomplished by using the methods to predict the specimen database and statistically evaluate the accuracy. Table 3 and Figure 8 illustrate a proposed approach to select the most accurate methods.

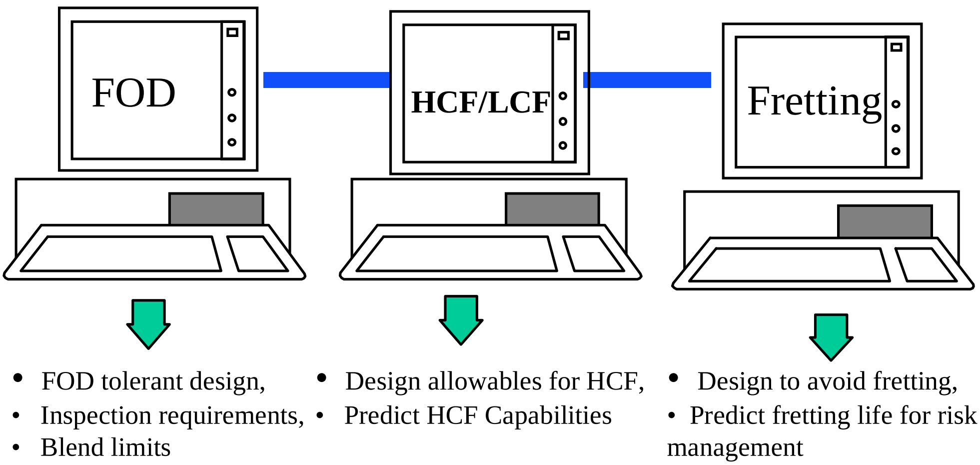

Figure 1. HCF/LCF Project to provide basic HCF methodology

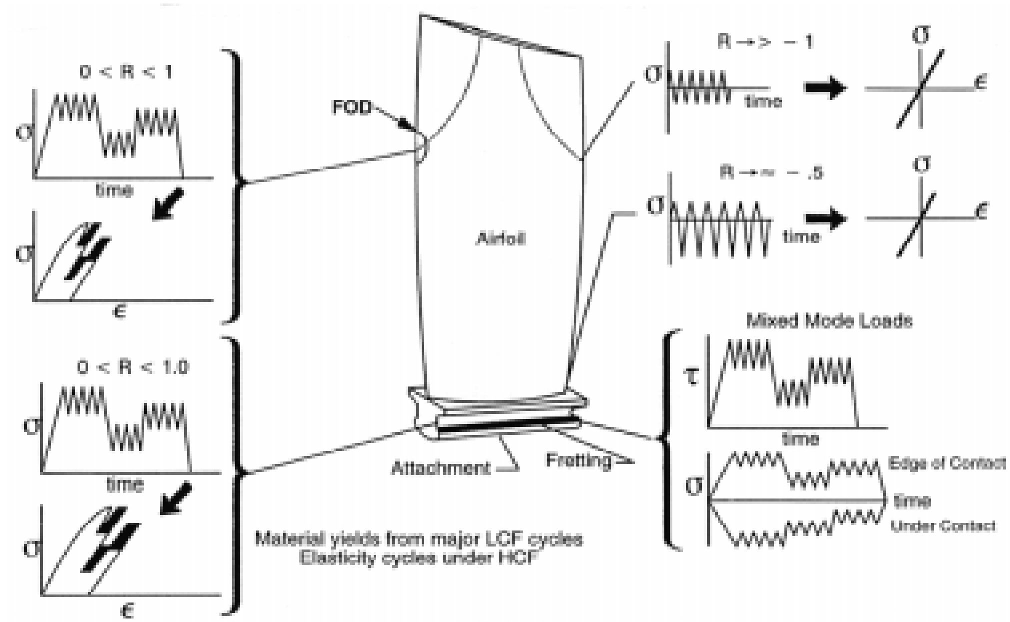

Figure 2 The complexity of blade HCF critical locations

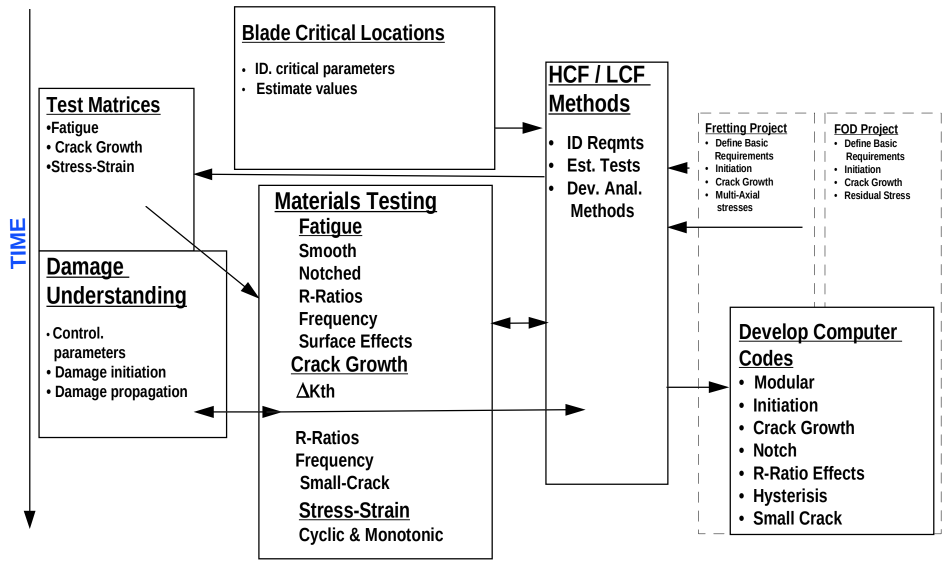

Figure 3 HCF/LCF Interaction strategy

Table 2 Presentations Relating to the HCF/LCF Damage State

Number of tests by type by organization										
			AADC	ASE	GEAE	P&W	SwRI	UDRI	UTRC	
HCF/LCF	Long Crack	Commonality			6	8				
		Threshold			6	8				
		Region II			12	4				
		Mission Effects				8				52
	Short Cracks	Smooth,no surface-R,str					2			
		Smooth-HCF/LCF					2			
		Smooth,surface - R					2			
		Notched-R					2			
		Notched-HCF/LCF					2			10
	Initiation,Smooth	R		64						
		Round robin			8	8	8			
		Frequency		32	24	8	16			
		Surface		48						
		Baseline LCF				16				
		Shotpeen LCF				16				248
	Initiation, Notched	R			5	69				
		Frequency					16			
		Kt					16			
		Surface				24				
		Baseline LCF				16				
		Shotpeened Lcf				16				162
	Initiation,LCF/HCF	Kt			4	4				
		Block-Smooth			2	2				
		Block-Notch			2	2				
		HCF/LCF Retardation			4	4				
		HCF/LCF Mechanism			15					39
	Stress-strain	Monotonic						8		
		Cyclic				8				16
		HCF/LCF Total		144	88	221	66	8		527

*The more detailed description of the test matrices for this project requires six page of space and cannot be shown within the confines of this document.

Table 2 Presentations Relating to the HCF/LCF Damage State

TYPE & TITLE	AUTHORS & AFFILIATION	WHERE/WHEN PRESENTED
Presentation – "The HCF/LCF Interaction Project in the PRDA V HCF materials and Life Methods Program"	R. deLaneuville, Pratt & Whitney	3rd National Turbine Engine High Cycle Fatigue Conference, San Antonio, TX, Feb 2-5, 1998
Presentation – "Rapid Generation of Goodman diagrams Using the Step Test Method"	R. Bellows, AlliedSignal engines	3rd National Turbine Engine High Cycle Fatigue Conference, San Antonio, TX, Feb 2-5, 1998
Presentation – "Correlation of Fracture surface Topography with Fatigue Load Spectrum"	T. Kobayashi, SRI International	3rd National Turbine Engine High Cycle Fatigue Conference, San Antonio, TX, Feb 2-5, 1998
Presentation – "Effect of Stress Relief Operation on Titanium Alloy Fatigue Behavior"	R. Bellows, Allied Signal Engines	3rd National Turbine Engine High Cycle Fatigue Conference, San Antonio, TX, Feb 2-5, 1998
Paper – "Effect of Step Testing and Notches on the Endurance Limit of Ti-6Al-4V"	Richard S. Bellows – Allied signal Engines, Ken Bain – GEAE Jerry Sheldon – Pratt & Whitney	Winter Annual Meeting of ASME in Anaheim, California November 15 – 20, 1998
Presentation – "Step Test, Stress Ratio and Surface Effects on the HCF of Ti-6-4	R. Bellows, Allied Signal engines, Paul R Smith, USAF, Daniel Eylon, UDRI	4th National Turbine Engine High Cycle Fatigue Conference, Monterey, CA, Feb 9-11, 1999
Paper – "Investigation of the Shed-rate, Initial K_{max}, and Geometric Constraint on ΔK_{th} in Ti-6Al-4V at RT"	Jerry Sheldon , Pratt & Whitney Ken R. Bain, GEAC, J. Keith Donald, Fracture Tech. Assoc.	Forthcoming publication of the International Journal of Fatigue
Presentation – "Fourier Analysis of Fracture Surface Topography to Deduce Fatigue Load Spectra"	Takao Kobayashi, SRI International, Donald Shockey, SRI International	4th National Turbine Engine High Cycle Fatigue Conference, Monterey, CA, Feb 9-11, 1999

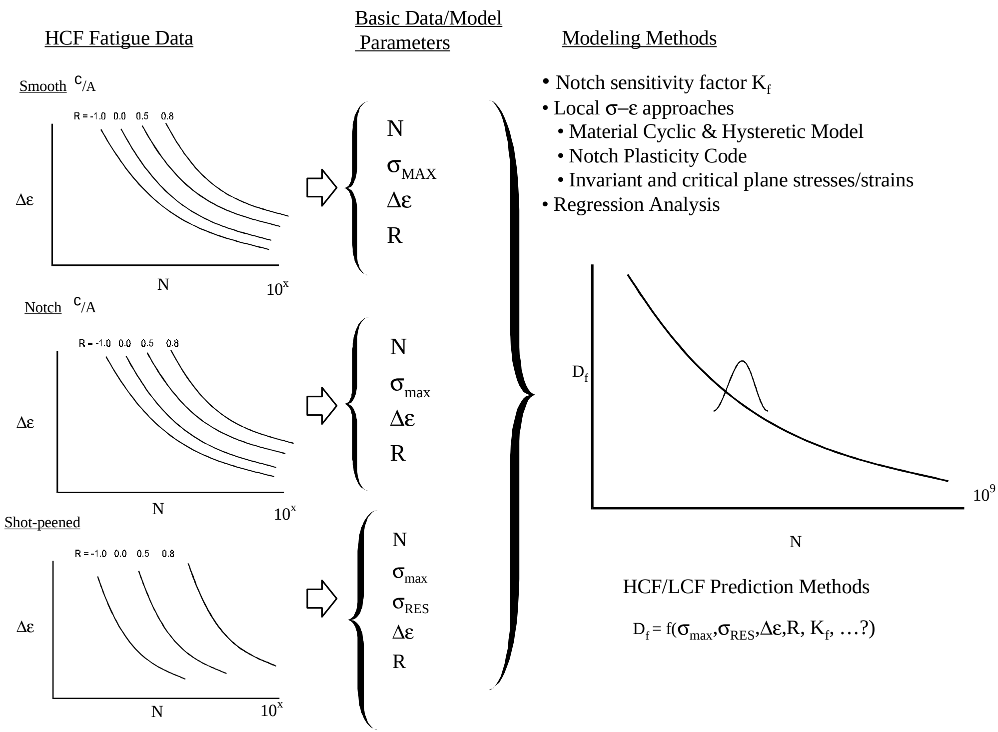

Figure 4 Approach to modeling smooth and notch fatigue data

Objective: Use local stresses and strains at the fatigue origin to predict HCF/LCF capabilities

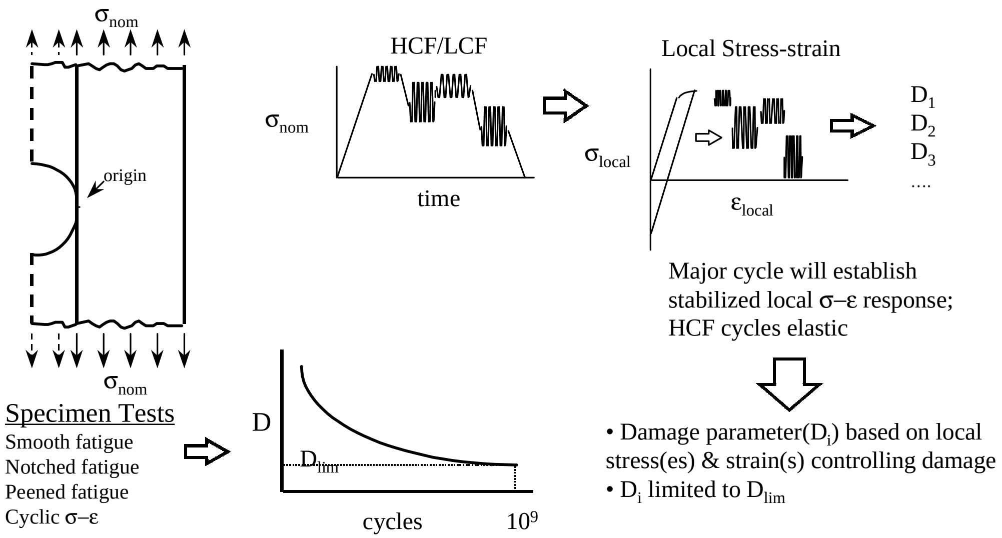

Figure 5 Approach to to modeling HCF/LCF interaction effects

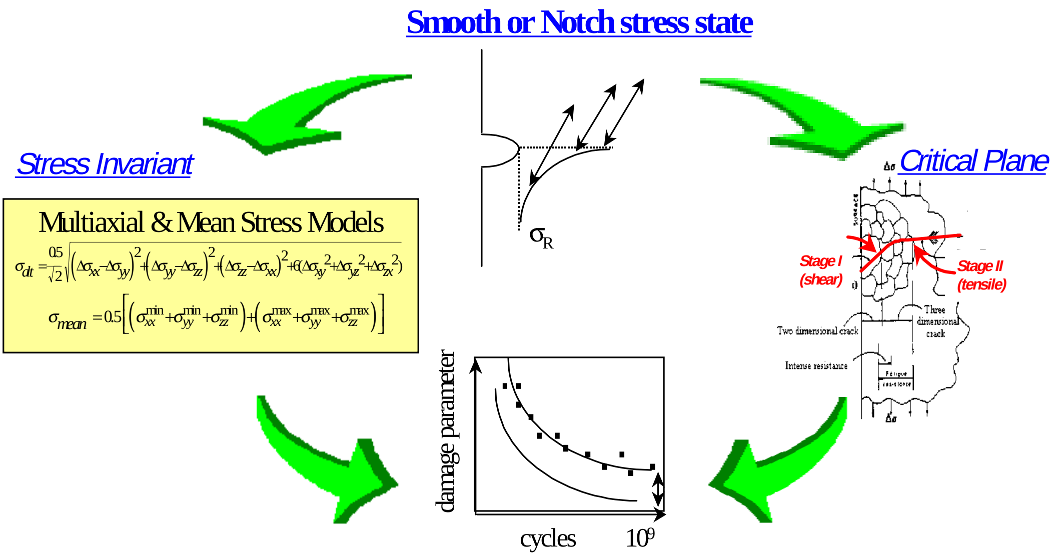

$$\sigma_{dt} = \frac{0.5}{\sqrt{2}}\sqrt{(\Delta\sigma_{xx}-\Delta\sigma_{yy})^2+(\Delta\sigma_{yy}-\Delta\sigma_{zz})^2+(\Delta\sigma_{zz}-\Delta\sigma_{xx})^2+6(\Delta\sigma_{xy}^2+\Delta\sigma_{yz}^2+\Delta\sigma_{zx}^2)}$$

$$\sigma_{mean} = 0.5\left[\left(\sigma_{xx}^{min}+\sigma_{yy}^{min}+\sigma_{zz}^{min}\right)+\left(\sigma_{xx}^{max}+\sigma_{yy}^{max}+\sigma_{zz}^{max}\right)\right]$$

Figure 6 Approach to evaluating local σ–ε methods with data

Figure 7

Model Crack growth rate data from threshold through Region II

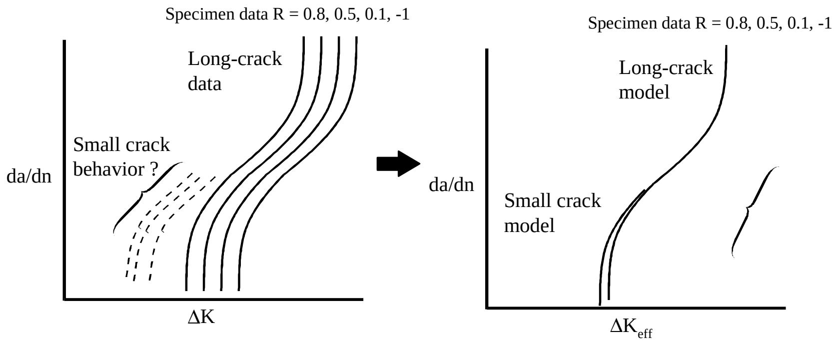

Model R-ratio behavior with ΔK_{eff} based on crack closure(P&W, Allison) and Walker exponent(GEAE)

Table 3

Perform a statistical analysis of each method individually,
and compare accuracy

(suggested example)

Specimen type		**Method 1**	**Method 2**	**Method 3**	
constant amplitude smooth		.89 (1.35)	1.00 (2.11)	.98 (1.91)	
constant amplitude notched		1.19 (2.67)	1.67 (3.20)	1.06 (2.21)	
HCF/LCF		1.45 (2.10)	1.53 (2.89)	1.02 (1.99)	
total		**1.18** **(2.04)**	**1.40** **(2.73)**	**1.02** **(2.03)**	

legend - A/P (B.1/B50. scatter)

Figure 8

Assess the model vs. the accuracy of predicting specimen behavior (plots and statistics) *(suggested example)*

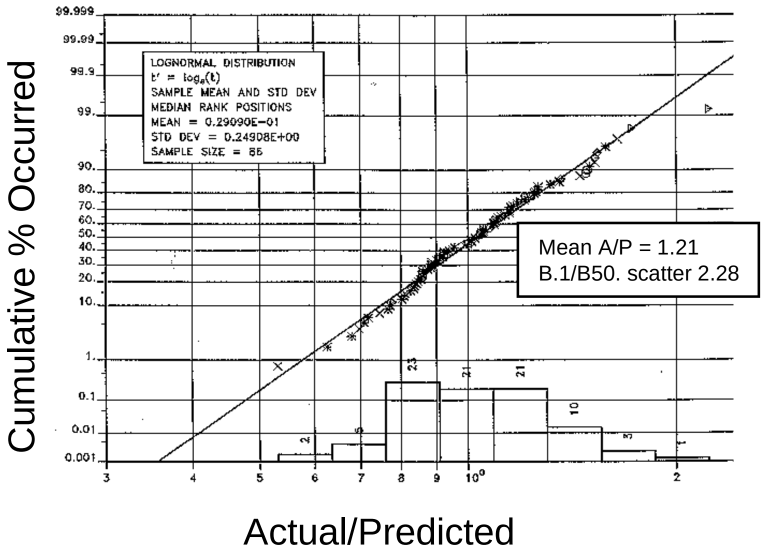

STEP TEST, STRESS RATIO AND SURFACE EFFECTS ON THE HIGH CYCLE FATIGUE BEHAVIOR OF Ti-6Al-4V

Dr. Richard Bellows*
AlliedSignal Engines, P.O Box 52181, Phoenix, AZ, 85018-2181
Mr. Paul Smith
Air Force Research Laboratory, 2230 Tenth St Ste. 1, WPAFB, OH, 45433-7817
Mr. Michael Shepard
Southwestern Ohio Council for Higher Education (SOCHE)
3171 Research Blvd., Dayton, OH 45420-4014
Dr. Daniel Eylon
University of Dayton, 300 College Park, Dayton, Ohio 45469-1679

ABSTRACT

The step test results of smooth bar Ti-6Al-4V fatigue specimens tested at four stress ratios are reviewed and compared to conventional fatigue test data. The statistical viability of the step test data has been demonstrated by using log-normal-based statistical methods. The step tests results at the four stress ratios lie within the three sigma limits of the conventional fatigue data endurance limit. However, the -1 stress ratio conventional data shows the greatest scatter, and the -1 step test results are near or above the endurance limit mean value. Possible explanations for the results at the -1 stress ratio are given. Second, conventional fatigue results from smooth bar Ti-6Al-4V specimens that were prepared using different manufacturing techniques (low stress grind plus polish, single point turned, or ground) are compared with results from baseline (stress-relieve plus chem-mill) specimens. Differences in fatigue behavior are discussed with respect to differences in surface residual stress levels and in surface roughness.

INTRODUCTION

The goal of the current Air Force High Cycle Fatigue (HCF) Improved Life Prediction Program is to improve life prediction capabilities for rotating titanium components in gas turbine engines. A primary cause of component failure in these engines is HCF, and HCF failures often occur in sequence with or simultaneously with other types of damage modes.[1,2] The development of damage tolerant life methodologies that take into account these damage modes, namely low cycle fatigue (LCF), foreign object damage (FOD) and fretting, necessitated the determination of endurance limits of damaged specimens. Since imparting identical damage to several specimens for the construction of a S-N curves can be difficult, not to mention expensive and timely, it was necessary to validate a test method that could determine an endurance limit from a single specimen. Thus, the step test method was recommended for validation at four stress ratios: 0.1, 0.5, 0.8 and -1. In addition, the effect of different surface conditions, similar to those of actual components imparted by different machining and processing conditions, on fatigue behavior needed to be evaluated and understood when developing HCF life methodologies.

EXPERIMENTAL

The specimens used in this study were excised from forgings that were representative of turbine engine fan blade forgings. The forging stock had been melted (double arc remelt) and converted (to 2.5 inch diameter billet followed by mill annealing at 1300°F/2 hours/air cool) in accordance with AMS4928. The billet, which was from a single heat of material, was inspected in accordance with AMS2631B (Class AA) and found acceptable. Forging multiples, 16 inches in length, were sectioned from the billet and preheated to 1720°F for at least one hour prior to press forging on glass lubricated warm dies to the final forging dimension of 16 by 6 by 0.8 inches. Forging were air cooled off the press and were sequentially numbered in the order of forging.

Although fan blade forgings are typically mill-annealed after forging, the forgings in this study were solution treated to maximize forging uniformity and minimize forging-to-forging variation. The solution temperature was selected to provide a relatively high primary alpha content (approximately 60%) that would be more representative of a mill-annealed microstructure (which can exceed 60% primary alpha content) rather than a solution-treated microstructure (which typically has 20 to 40% primary alpha content). Because of the large number of forgings used in the program, four separate solution treatment batches were used.

After solution treating, all of the solution treated forgings were cleaned of oxide and alpha case using caustic and acid baths as well as grit blasting. Then the forgings were vacuum-annealed (often considered an overaging after solution treatment) at 1300°F for 2 hours at temperature to stabilize the microstructure and normalize the hydrogen content. Vacuum annealing was accomplished in two lots. The typical forging microstructure, which contains approximately 60% primary alpha with the remainder transformed lamellar alpha-beta structure, is shown in Figure 1.

The specimens used in this study had a gage diameter of 0.20 inches and a uniform gage length of 0.75 inches. The specimens were excised so that the specimen axis was always parallel to longest dimension of the forging. The standard baseline specimens were low stress ground and longitudinally polished, followed by vacuum stress relieve anneal to remove machining residual stresses, followed by chem-milling to remove approximately 0.001 inch of material from the gage surface to ensure freedom from surface contamination. Surface effects specimens, with the exception of shot peened specimens, were stress relieved prior to machining in order to achieve a consistent metallurgical state. After stress relief, the surface effects specimens were either low stress ground and longitudinally polished, single point turned, or ground to produce different surface finishes. Shot peened specimens were manufactured per the standard baseline condition but will be shot peened after completing chem milling. All tests were run on a servo-hydraulic, closed-loop test frame under load control conditions at 60Hz and room temperature in lab air.

Conventional tests were considered run-outs (suspended) after 10 million cycles. When step tests [3] were run, a single specimen was subjected to blocks of 10 million cycles. If failure did not occur during the step test block of 10 million cycles, the stress ratio, temperature and frequency were kept constant, but the stress range was increased by a set percentage (either 3 or 5%). Another block of 10 million cycles was run using the same specimen at the higher stress range. The same specimen would be subjected to blocks of 10 million cycles with increasing stress ranges until failure occurred (see Figure 2). The 10 million cycle endurance stress was calculated using

$$\sigma_{ES} = \sigma_{PS} + (\sigma_F - \sigma_{PS})\, N_f / 10^7 \quad \ldots\ldots\ldots\ldots\ldots\ldots\ldots\ldots\ldots\ldots(1)$$

where σ_{ES} is the constant life endurance stress, σ_{PS} is the stress from prior unfailed block, σ_F is the stress from final block, and N_f is the cycles to failure in final block.

The conventional and step test results were statistically analyzed using the following method[4]. Power law curves were fit to the unsuspended conventional data (i.e., conventional run-outs were not included). A bi-linear power law fit was used for the -1 data. Next, the conventional failures between 1 and 10 million were extrapolated to 10 million cycles using the slope of the power law curve, as shown in Figure 3. For some stress ratios, it was necessary to extrapolate points to the left of 1 million cycles. The extrapolated values, which were now considered failures at 10 million cycles, were taken along with the conventional run-outs, which were considered suspensions at 10 million cycles, and a log-normal distribution was used to calculate the $+3\sigma$ and -3σ values for a 50 % confidence level for the 10 million cycle endurance limit as shown in Figure 4.

When performed, mid-gage x-ray residual stress measurements were made at the surface in the axial and circumferential directions and at nominal depths of 0.0005, 0.001, 0.003, 0.005 and 0.007 inches below the surface in the circumferential direction. Axial measurements at the nominal depths were not made because of the difficulty in making these measurements. These measurements were made in accordance with SAE J784. Material was removed electrolytically for sub-surface measurements, and the corrections for radiation penetration and stress relaxation caused by layer removal were applied as appropriate[5].

RESULTS AND DISCUSSION

Step Test and Stress Ratio Effects

The conventional and step test data are shown for the four stress ratios in Figure 5. Also shown are the $+3\sigma$ and -3σ values for the conventional tests. The step test results at the 0.1, 0.5 and 0.8 stress ratios are in good agreement with power law curve and fall within the relatively tight $+3\sigma$ and -3σ values established for each stress ratio. The step test results at the -1 stress ratio lie near or above the power law curve. At this stress ratio, the $+3\sigma$ and -3σ values for the conventional tests are quite wide, and one step test result appears to be very close to the $+3\sigma$ value. The corresponding Haigh (or modified-Goodman) diagram is shown in Figure 6.

Two easily observed characteristics of the -1 stress ratio data that are not shared by the 0.1, 0.5 and 0.8 stress ratio data are a high degree of scatter in the -1 stress range data and higher endurance values for the -1 stress ratio step test data.

There are several possible explanations for the scatter observed at -1 stress ratio. Surface contamination, surface defects or internal defects could cause differences in specimens lives. However, the near-surface microstructures were normal (Figure 7a), the gage surfaces near initiation appeared normal (Figure 7b), and the fracture surfaces of these specimens did not appear to have any defects (Figure 7c). When the -1 stress ratio data were plotted with reference to the three individual forgings from which they were excised, there did appear to be a stratification of the data with respect to the parent forging (Figure 8).

Specimens from forging number 108 appear to have relatively lower fatigue strengths when compared to specimens from forgings 26 and 149. Although all the forgings in the study came from the same heat (ingot) of material, variations within a single heat of material can occur because of the partitioning of elements to either the liquid or solid phase during vacuum arc remelting. These chemistry differences can manifest themselves as differences in strength as well as microstructure, since chemistry has a strong influence on the beta transus temperature. Differences in billet and forging textures and macrostructures can arise because of differences in cooling rates in the ingot or differences in conversion. Macrostructures can influence the size of the primary alpha and transformed beta colonies thereby influencing fatigue properties, and texture is known to have a strong influence on both modulus and fatigue strength. Heat treatment can give rise to differences in microstructure, including the primary alpha size, primary alpha volume fraction, transformed lamella thickness and lamella alignment. Thus, there are many ways for forgings to differ from each other. Even if the forgings were identical, specimens may be excised from the forging at slightly different angles that could give slightly different textures that could affect fatigue properties[6]. While there are many reasons why individual forgings can vary, it is important to note that the specimens used for the other three stress ratios came from the same three forgings but did not produce the same degree of scatter at these other stress ratios.

It is possible that materials may become more sensitive at lower maximum stresses (the -1 data had the lowest maximum stress levels). Unpublished high cycle fatigue data for HIPed (treated by hot isostatic pressure to close and seal internal porosity) and un-HIPed single crystal, nickel-base superalloy castings show that at higher maximum stress levels, there is essentially no difference between HIPed and unHIPed single crystals. Only as the stress ratio becomes less positive (and the maximum stress becomes lower) does the beneficial effect of HIP become evident. It appears that at higher maximum stress levels, initiation at pores and surface/subsurface initiation are competitive, but at lower maximum stress levels, initiation and failure from internal porosity controls life. That is, at lower maximum stress levels, the material becomes more sensitive to microstructural differences.

In alpha-beta processed Ti-6-4, the controlling microstructural constituent can be the primary alpha particle[7]. Two factors that may determine whether a primary alpha particle will initiate a crack are size of the primary alpha particle (determine by degree of mechanical work performed during converting and forming and by heat treatment) and orientation of the primary alpha particle (determined by the orientation of the prior beta grain via the Burgers relationship). The orientation of the primary alpha particle with respect to stress determines the resolved shear stress for a particular crystallographic plane and crystallographic direction. The size of the primary alpha particle controls the plastic shear strain since the plastic shear strain is a function of dislocation density, Burgers vector and average length that dislocations travel. Therefore, there will be some distribution of primary alpha particles that, because of their orientation, will experience slip; likewise, there will be some distribution of primary alpha size where larger alpha grains will experience greater plastic shear strain. When these two factors occur in the same primary alpha particle, that primary alpha particle will incur greater amounts of strain than other particles. This shear strain must be accommodated in an adjacent grain or cracking may occur. Figure 9 is a SEM photo of an electropolished specimen subjected to fatigue. Just below the fracture surface, near the initiation site, a primary alpha particle can be seen with approximately parallel slip lines running through it. The other alpha particles in the area do not show this type of slip line activity. When the slip line gets to the beta phase, the angle changes and slip continues into the next alpha particle. Towards the edge of the fracture surface, the slip lines do not propagate into the adjacent microstructure, and a crack has formed between the primary alpha particle with slip line and between the adjacent beta phase. While this may not have been the initiation point for this specimen's failure, a similar situation in a nearby location may have been. In some cases, the transformed lamellar colonies may act as a single slip system and cause failure. Regardless of the crack initiation mechanism, the activation of the mechanism could become more metallurgically sensitive at lower maximum stress conditions.

Possible explanations for the step test results at -1 stress ratio resulting in a higher endurance limits could be related to coaxing or statistical selectivity. Coaxing is the reported increase in the endurance strength of materials that have been cycled at lower stresses below the endurance limit. If it is occurring in this study, it did not occur at the other stress ratios and did not occur consistently among the -1 stress ratio step test specimens. Statistical selectivity[8] is the elimination of lower strength specimens as failures, which leaves the higher strength specimens to survive and become step test candidates. Figure 10 illustrates this possibility. Indeed, statistical selectivity would have a more observable effect on populations that have more scatter, as the -1 data appeared to have.

<u>Surface Effects</u>

SEM photographs of the surface conditions of the first three surface effect groups are shown in Figures 11 and 12. Delivery of the fourth group (shot peened) was delayed, and results could not be included. At low magnification, the surface of each conditions appear uniform. The single point turned specimen appears to have the most pronounced surface texture. At higher magnification, all three conditions appear to have pronounced surface texture. The low stress ground and longitudinally polished ((LSG+LP) specimen and the ground (GRD) specimen both exhibit a fair amount of smeared metal.

The residual stresses measured in the axial and circumferential direction are shown in Figure 13. Although the axial residual stresses would appear to have the greatest effect on fatigue strength, accurate measurements in the axial direction of cylindrical gages can be difficult and are much less repeatable than in the circumferential direction. Therefore, the circumferential direction measurements were taken as a function of depth The greatest compressive residual stresses on the surface in the axial direction were measured on the single point turned (SPT) specimen. The compressive residual stresses on the surface in the circumferential direction measured on the ground (GRD) specimen were slightly greater than that measured on the SPT specimen, but the SPT specimen had higher compressive residual stresses measured below the surface.

The fatigue results for the surface effect specimens are shown in Figure 14. In general, the three groups of surface effects specimens show greater fatigue resistance than the baseline group of specimens at 0.1 and -1 stress ratios, and the -1 stress ratio (lower maximum stress) data may be the most sensitive to surface effects. However, at 0.8 there does not appear to be any significant difference between the three groups of surface effects specimens and the baseline specimens. It may be that the residual stresses at the 0.8 stress ratio are “stress relieved” by the large maximum stress levels at this stress ratio which causes the specimens to creep or ratchet with permanent displacements.[9] Additional work will include shot peen specimen testing, post-test residual stress measurements, and fractographic examination.

SUMMARY

The step test method is valid for determining endurance limits. At lower maximum stress levels (e.g., -1 stress ratio), there is inherently more scatter, most likely as a result of increased sensitivity to metallurgical parameters and texture differences. With more scatter, step test results may appear to give higher endurance levels because of the elimination of weaker specimens through statistical selectivity.

Surface preparation can impart surface and near-surface residual stresses that can affect fatigue properties. At higher stress ratios (i.e., 0.8 stress ratio), the beneficial effect of residual compressive stresses is not observed. Specimens tested at lower maximum stress levels (-1 stress ratio) may be the most sensitive to surface effects, as well other metallurgical differences.

ACKNOWLEDGEMENTS

The support of the Air Force is gratefully acknowledged. Much of this work was performed as part of the Improved High Cycle Fatigue (HCF) Life Prediction Program, USAF Contract #F33615-96-C-5269. The collaborative efforts of the following team members are appreciated: University of Dayton Research Institute, Allison Advanced Development Company, General Electric Aircraft Engines, Pratt & Whitney, and Southwest Research Institute.

REFERENCES
1. Cowles, B.A., *International Journal of Fatigue,* Vol. 80, 1996, pp. 147-163.
2. Nicholas, T. and J.R. Zuiker, *International Journal of Fatigue,* Vol. 80, 1996, pp. 219-235.
3. Maxwell, D.C and T. Nicholas, ASTM STP1321, 1998.
4. Bellows, R.S. , S. Muju and T. Nicholas, *International Journal of Fatigue*, accepted for publication, 1998.
5. Lambda Research Report #54-8401, 1998.
6. Peters, M., A. Gysler and G. Lutjering, *Metallurgical Transactions A*, Vol.15A, 1984, pp.1597-1605.
7. Gilbert, J.L. and H.R. Piehler, *Metallurgical Transactions A*, Vol.24A, 1993, pp 669-680.
8. Epremian, E. and R.F. Mehl, ASTM STP 137, 1952.
9. Morrissey, R. J., Report # WL-TR-97-4100, 1997.

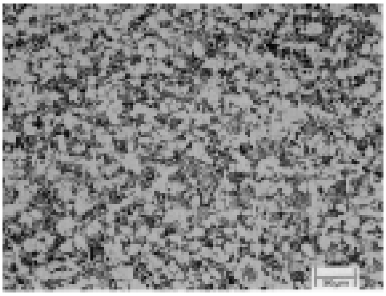

FIGURE 1. The typical forging microstructure (60% primary alpha).

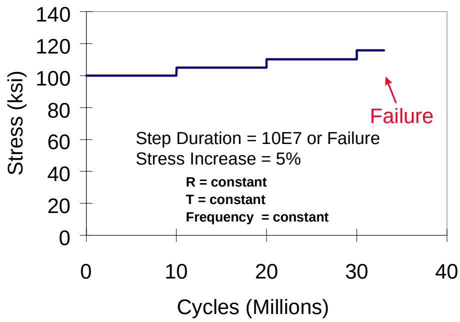

FIGURE 2. Schematic showing how step testing was accomplished.

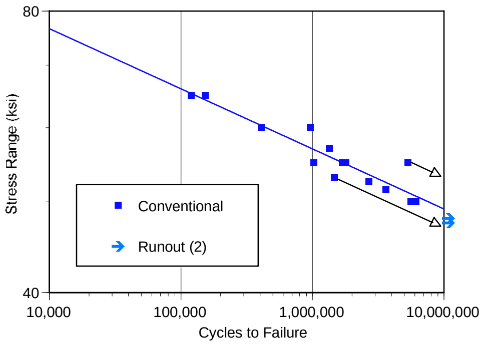

FIGURE 3. Conventional test failures were extrapolated to 10 million cycles in determining scatter.

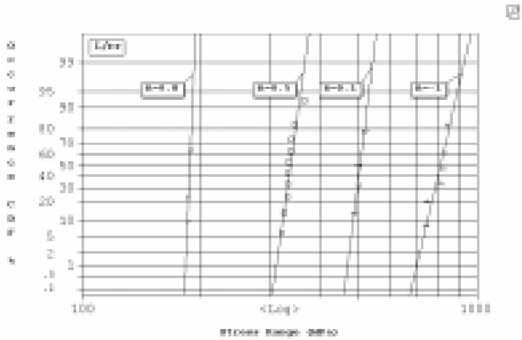

FIGURE 4. Log-normal distributions were used to calculate 3 sigma values.

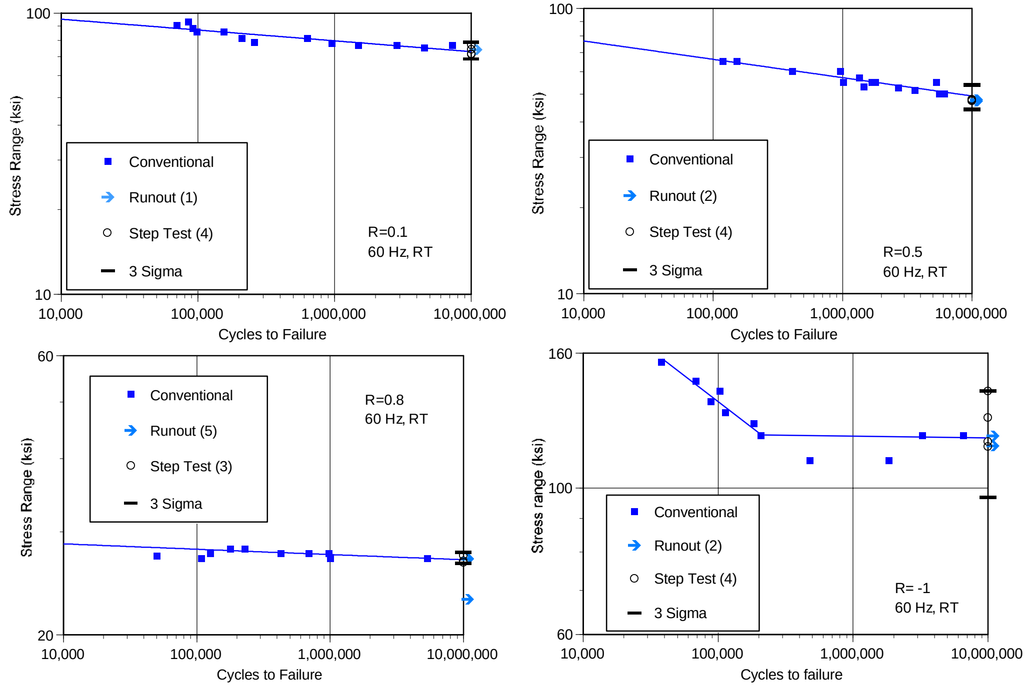

FIGURE 5. The conventional and step test data for the four R ratios.

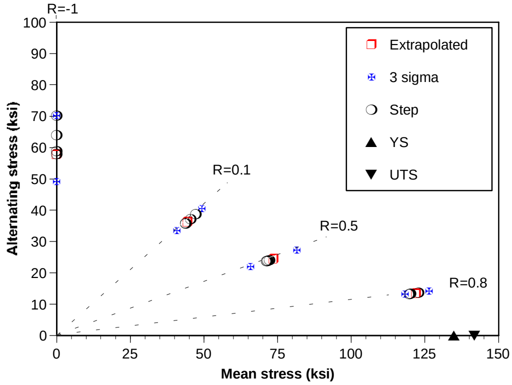

FIGURE 6. The Haigh diagram comparing the extrapolated endurance limits (and corresponding 3 sigma values) and the step test results at 10 million cycles.

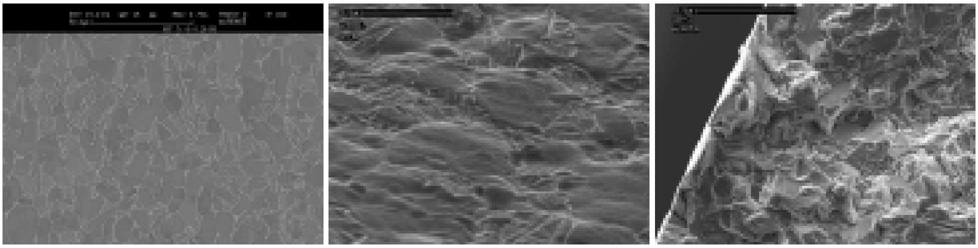

FIGURE 7. Near fracture-surface microsturctures, gage surfaces and fracture surfaces all appeared normal.

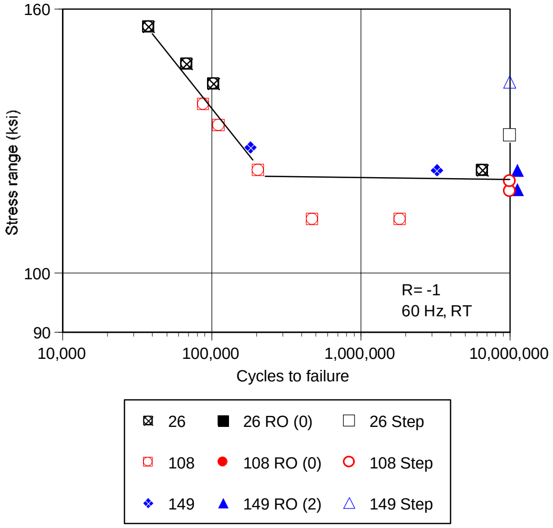

FIGURE 8. Data at -1 stress ratio identified by the parent forging number.

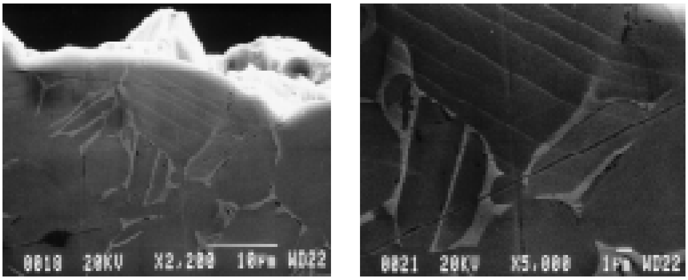

FIGURE 9. SEM photo of an electropolished specimen subjected to fatigue showing a primary alpha particle with slip lines.

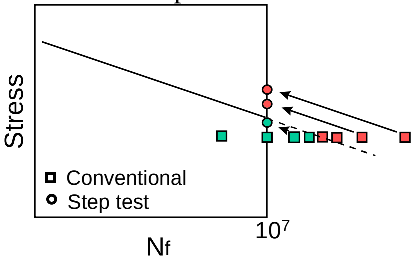

FIGURE 10. Schematic of how statistical selectivity would provide higher step test endurance limits on populations with fatigue strength scatter.

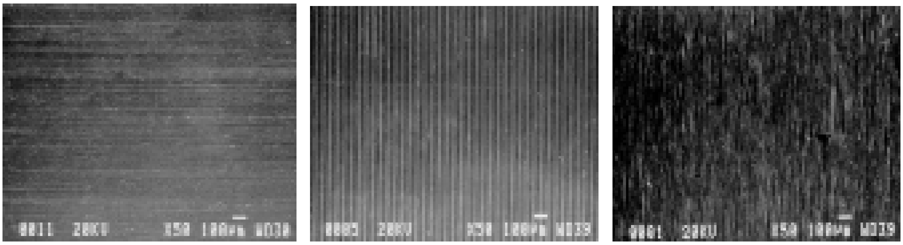

FIGURE 11. Low magnification photos of the surface effect specimens (LSG+LP, SPT and GRD, from left to right).

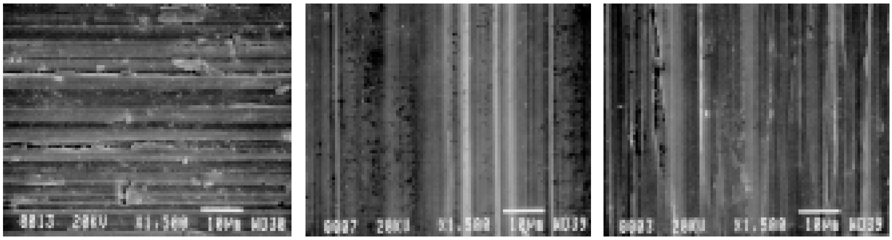

FIGURE 12. High magnification photos of the surface effect specimens (LSG+LP, SPT and GRD, from left to right).

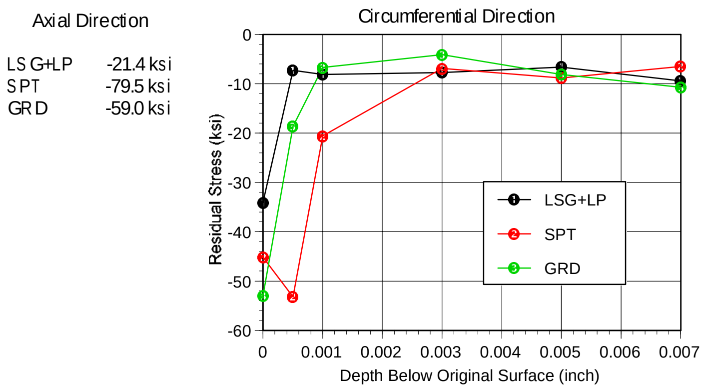

FIGURE 13. Residual stresses as measured in the surface effect specimens.

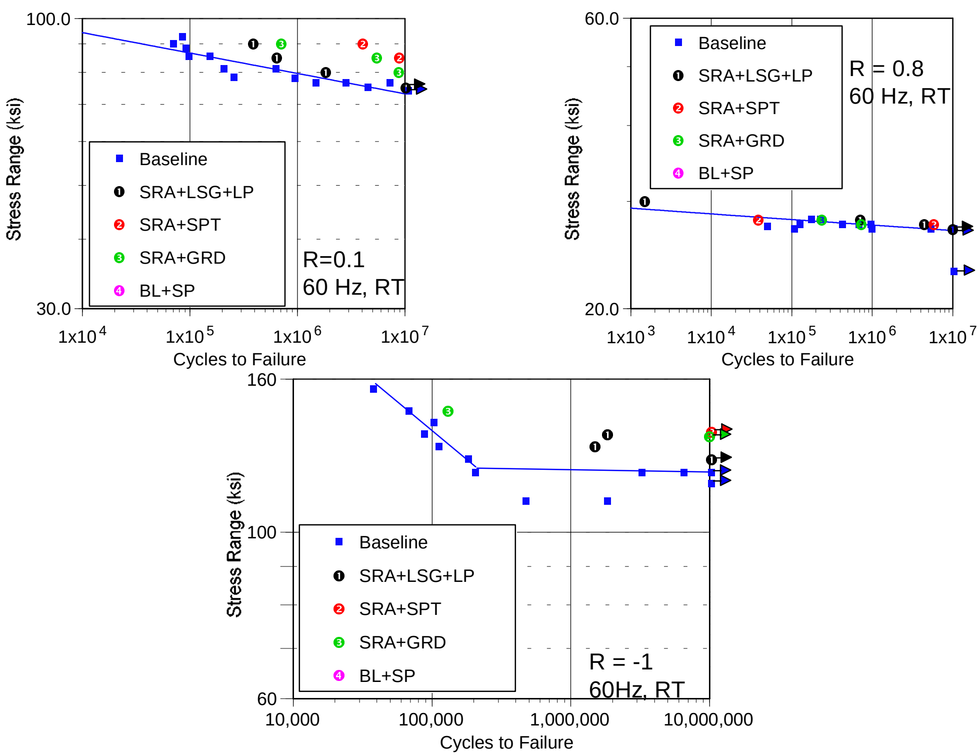

FIGURE 14. High cycle fatigue results of the surface effects specimens.

High Cycle Fatigue of Nickel-Base Superalloys

Mr. Santo A. Padula II
Graduate Student

Mr. Amit Shyam
Graduate Student

Dr. Walter W. Milligan*
Professor
Department of Metallurgical and Materials Engineering
Michigan Technological University
Houghton, MI 49931-1295

Introduction

This paper and presentation represent the first two years of progress on a project funded by the Air Force Office of Scientific Research (AFOSR) Multi-University Research Initiative (MURI) program. The MURI is based at the University of California-Berkeley, with Professor Robert O. Ritchie as principal investigator. The research efforts at Michigan Tech focus on high temperature nickel-base superalloys, while the efforts at Berkeley are aimed at low temperature titanium alloys. The MURI also includes a program based at MIT on fretting (Subra Suresh, principal investigator), and a program based at Harvard on novel sensors and mechanics modeling (John Hutchinson and Anthony Evans, principal investigators.)

In the second year of the project, a 1,000 Hz servohydraulic fatigue testing system was perfected, and fatigue crack propagation tests were conducted at both room temperature and at 650^{o}C on a nickel-base turbine disk alloy. Additionally, in situ SEM experiments were conducted in collaboration with Southwest Research Institute on a single crystal blade alloy.

Materials and Procedures

The majority of the testing has been accomplished on KM4, a powder metallurgy disk alloy with a microstructure which is very similar to commercial alloys. It was developed under the NASA Enabling Propulsion Materials (EPM) program, specifically to resist hold time fatigue crack propagation at intermediate temperatures (around 650^{o}C, representative of the critical locations in the turbine disks.) Its chemical composition is nominally the following (in weight percent): 18 Co, 12 Cr, 4 Mo, 4 Al, 4 Ti, 2 Nb, and 0.03 C, B and Zr. Two heat treatement were investigated, one which resulted in a grain size of 5 microns, and another which resulted in a grain size of 55 microns. The microstructures are documented in the proceedings of the 1998 HCF conference. In situ tests were conducted on Rene N5, GE's single crystal blade alloy.

Tests were conducted at 50 and 1,000 Hz at a variety of load ratios. Tests were conducted in four-point bending, using an induction heater for the high temperature tests. In situ tests were conducted at about 2 kHz in the SwRI loading stage, again at a variety of load ratios.

Results - KM4

Most of these results are in press in Reference [1]. It was demonstrated in this work and the Berkeley work that there was no effect of frequency on FCP behavior between 50 and 1,000 Hz.

Figure 1 shows the results of microstructure on FCP behavior of KM4 at R=0.7. It is evident that the supersolvus material, with the higher grain size, had a higher crack propagation threshold.

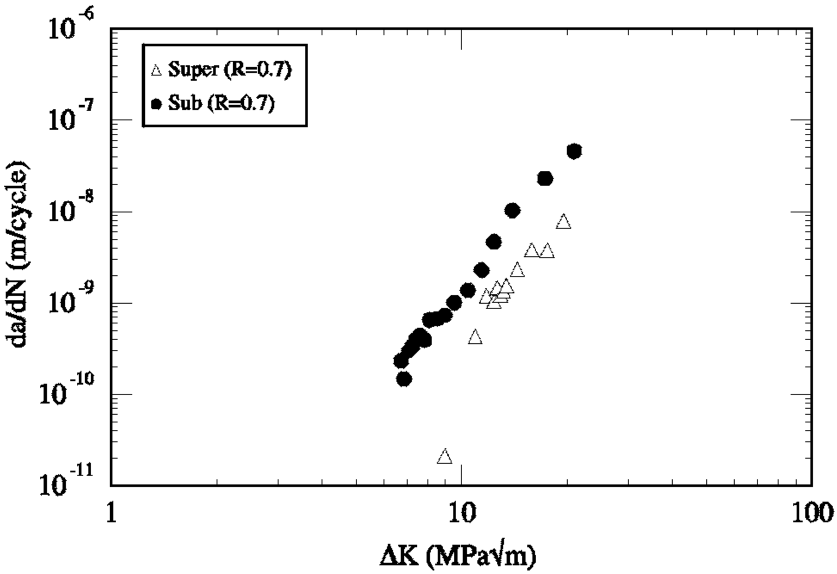

Figure 1. Da/dN vs. ΔK for KM4 as a function of grain size. Sub-solvus material has 5 micron grain size, super has 55 microns.

Figures 2 and 3 shows the effects of load ratio on fatigue behavior of KM4 at 1,000 Hz. For both microstructures, increasing R decreases the threshold.

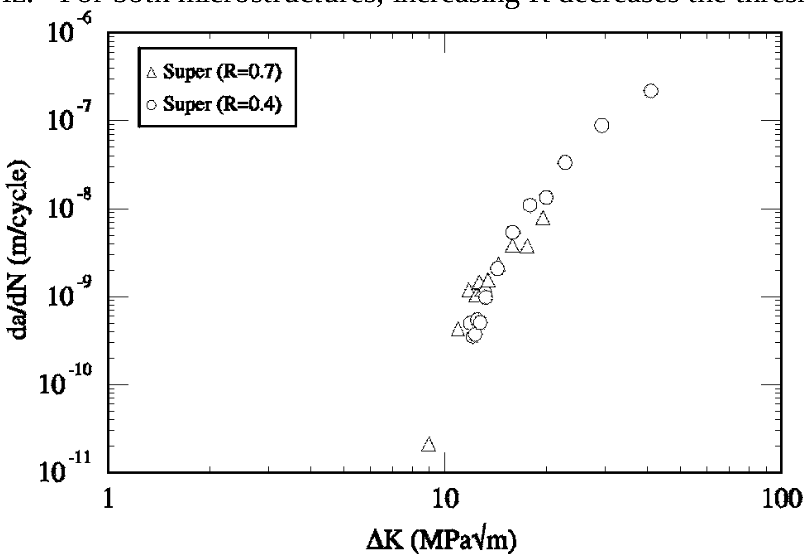

Figure 2. Da/dN vs. ΔK for KM4 at different R ratios.

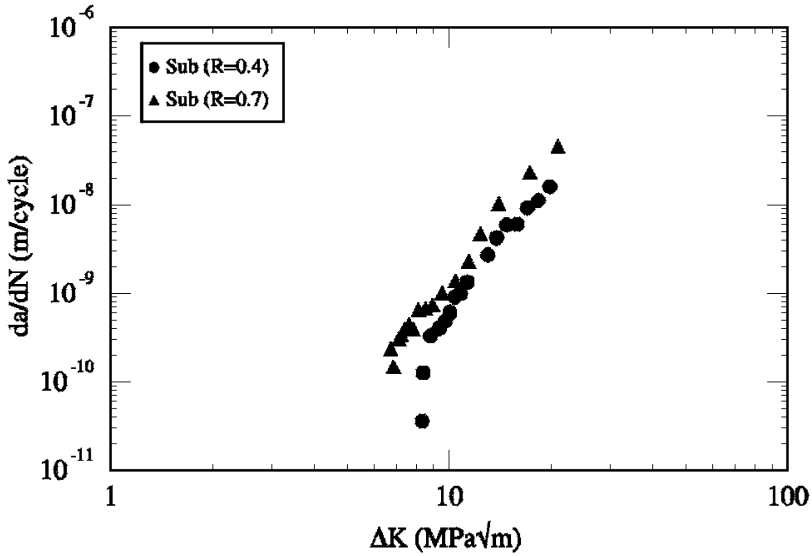

Figure 3. Da/dN vs. ΔK for KM4 at different R ratios.

The effects of microstructure are accompanied by changes in the crack morphology. As shown in Figures 4 and 5, the fine-grained material had a much smoother crack path and smaller facet sizes, while the coarser-grained super-solvus material had much more crack path tortuosity. The changes in threshold as well as the fractography are fully consistent with earlier studies on similar alloys conducted at 50 Hz, as discussed in [1].

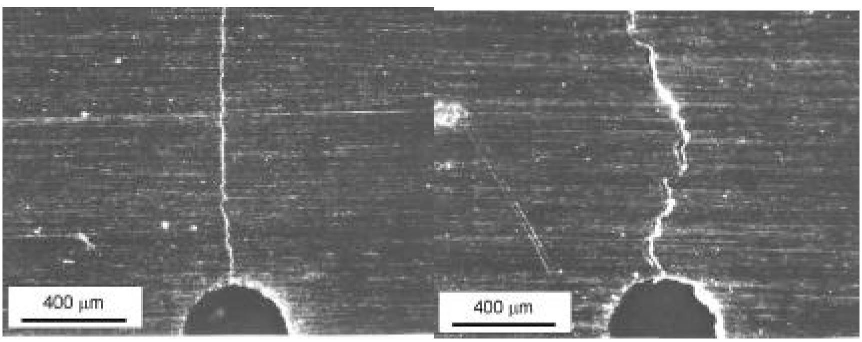

Sub-solvus (5μm g.s.) Super-solvus (55mm g.s.)

Figure 4. Optical micrographs of crack paths as a function of grain size.

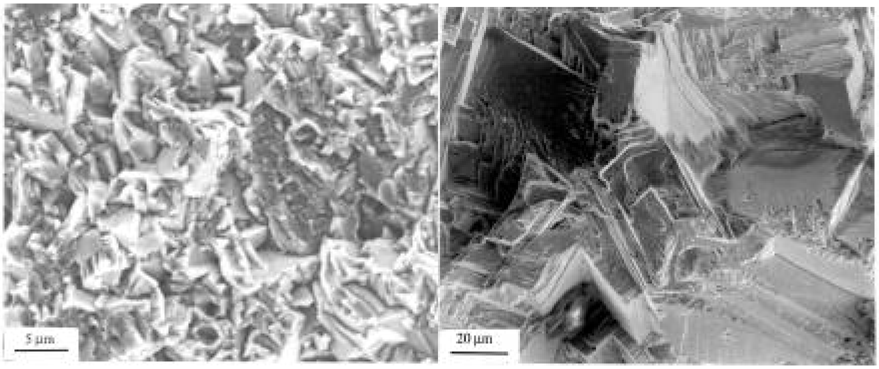

Sub-solvus (5µm g.s.)   Super-solvus (55mm g.s.)

Figure 5. Scanning electron micrographs of fracture surfaces as a function of grain size.

Figure 6 shows preliminary results of FCP behavior of KM4 at 650°C. The data is in the Paris regime, and lines up well with GE data at 50 Hz, at a lower temperature (which should be expected to give similar response). The majority of the future work will concentrate on the high temperature regime.

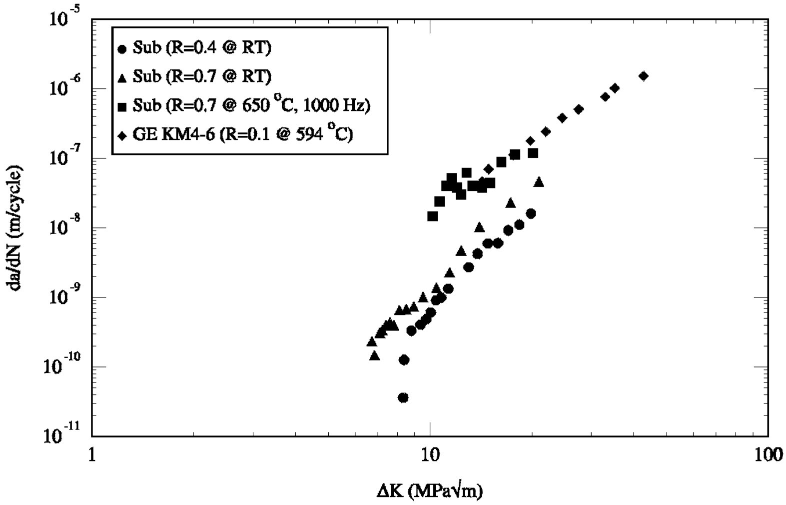

Figure 6. Da/dN vs. ΔK for KM4 at room temperature and 650°C.

Results - In Situ Behavior of Rene N5

Rene N5 single crystals were tested in the SwRI 2 kHz loading stage SEM. Tests were conducted at several load ratios. Near-threshold FCP behavior is shown in Figure 7, in comparison with the KM4. It is evident that the lack of grain boundaries has led to a decreasing threshold, since the fine scale microstructures of N5 and KM4 are similar.

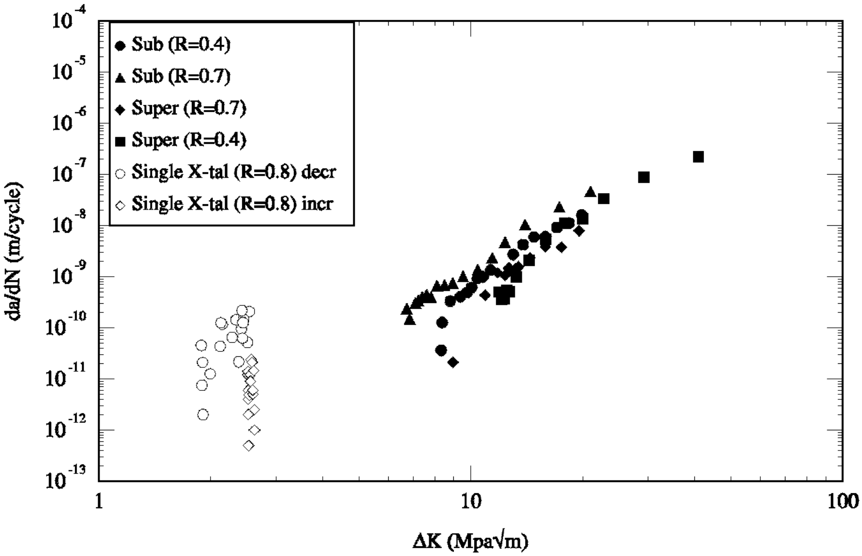

Figure 7. Da/dN vs. ΔK for Rene N5 at room temperature.

Figure 8 shows SEM micrographs taken during unloading of the N5 specimens at different ΔK levels. At the lowest ΔK level, near threshold, step-wise crack growth on {001} planes is evident, as shown earlier by Telesman at NASA-Lewis. Note the absence of shear bands. At a slightly higher ΔK level, shear bands and {111} crack growth are observed. It is apparent that the lack of shear bands and the crack growth modes are related to each other, and studies of thiese phenomena are in progress.

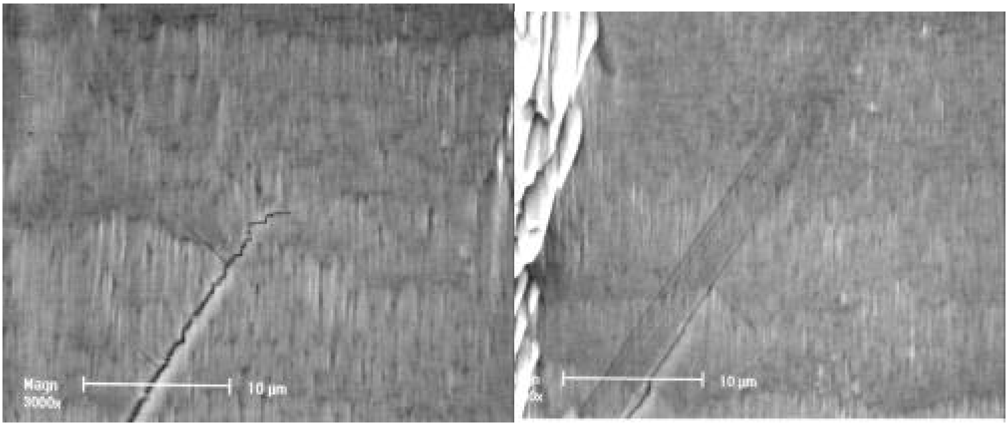

(a) (b)

Figure 8. Scanning electron micrographs specimen surfaces during in situ crack growth of Rene N5. (a) Near threshold, $\Delta k = 2.2$ MPa√m, showing step-wise propagation on {001} planes and no shear bands. (b) $\Delta k = 3$ MPa√m, showing shear bands and propagation along {111} planes.

Conclusions

Room temperature FCP tests on KM4 at 1,000 Hz verified earlier trends found at 50 Hz in similar alloys. High temperature testing at 1,000 Hz has been achieved, and in situ studies of single crystals are being analyzed currently. High temperature testing will be the focus of the remainder of the program.

Reference

[1] S.A.Padula II, A. Shyam, R.O. Ritchie, W.W. Milligan, "High Frequency Fatigue Behavior of a Nickel-Base Turbine Disk Alloy", International Journal of Fatigue, accepted, in press.

03/11/99 1:28 PM
Report No. UCB/R/98/

Department of Materials Science and Mineral Engineering
University of California at Berkeley

ON THE DEFINITION OF LOWER-BOUND FATIGUE-CRACK PROPAGATION THRESHOLDS IN Ti-6Al-4V UNDER HIGH CYCLE FATIGUE CONDITIONS

B. L. Boyce[*] and R. O. Ritchie

Department of Materials Science and Mineral Engineering
University of California, Berkeley, CA 94720-1760

to be presented at the
4th *National Turbine Engine High Cycle Fatigue Conference*
Monterey, California, Feb.1999

February 1999

Work supported by the U.S. Air Force Office of Scientific Research under Grant No. F49620-96-1-0478 under the auspices of the Multidisciplinary University Research Initiative on *High Cycle Fatigue* to the University of California.

ON THE DEFINITION OF LOWER-BOUND FATIGUE-CRACK PROPAGATION THRESHOLDS IN Ti-6Al-4V UNDER HIGH CYCLE FATIGUE CONDITIONS

B. L. Boyce* and R. O. Ritchie
Department of Materials Science and Mineral Engineering
University of California, Berkeley, CA 94720-1760

Abstract - Microstructural damage that can cause fatigue-crack growth under high-cycle fatigue loading is critical issue in the lifetime prediction of turbine-engine components. The extremely high cyclic frequencies typical of in-flight loading and the presence of small cracks resulting from fretting or foreign object damage (FOD) necessitate that a defect-tolerant design approach be based on a crack-propagation threshold. The present study is focused on characterizing such near-threshold fatigue-crack growth in a Ti-6Al-4V blade alloy at high load ratios and frequencies. Results indicate that "worst-case" large-crack thresholds may be used as a *practical* lower bound to describe the onset of small-crack growth from natural initiation and FOD sites.

INTRODUCTION

High-cycle fatigue (HCF) is one of the prime causes of turbine engine failure in military aircraft [1]. It can result in essentially unpredictable failures due to the growth of fatigue cracks in blade and disks under ultrahigh frequency loading, where the cracking initiates from small defects often associated with microstructural damage caused by fretting or foreign object impacts [2]. To prevent HCF failures, methodologies are required that identify the microstructural damage which can lead to such failures. This paper is focused on the critical levels of damage in a Ti-6Al-4V alloy, typically used in the front, low-temperature stages of the engine.

During HCF, engine components experience high frequency (~1-2 kHz) vibrational loads due to resonant airflow dynamics, often superimposed on a high mean stress [2,3]. Because of the high frequencies, HCF-critical turbine components must be operated below the fatigue-crack propagation threshold (ΔK_{TH}) such that crack propagation *cannot occur* within ~10^9 cycles. Although an extensive database [4,5] exists for such thresholds, it has been derived mainly from test geometries containing large (> few mm) cracks, often under loading conditions that may not be representative of turbine-engine HCF. Furthermore, except under specific loading conditions, e.g., at very high mean loads, such tests are not necessarily relevant to the HCF problem, where the critical flaw sizes are much smaller, i.e., < 500 μm [6]. Since small cracks can grow at velocities faster than corresponding large cracks (at the same *applied* stress intensity) and can propagate *below* the large-crack ΔK_{TH} threshold, design against HCF failure must be based on the notion of a practical small-crack threshold, measured under the representative conditions [7].

Small cracks appear to behave differently from large cracks when crack sizes become comparable to i) microstructural size scales, where biased sampling of the micro-structure leads to accelerated crack advance along "weak" paths (continuum limitation), ii) the extent of local plasticity *ahead* of the crack tip, where the assumption of small-scale yielding implicit in the use of K is not strictly valid (linear-elastic fracture mechanics limitation), or iii) the extent of crack-tip shielding *behind* the crack tip, where the reduced role of shielding leads to a higher *local* driving force than for the equivalent large crack at the same applied ΔK (similitude limitation) [8]. Of these cases, the latter is most important in the present case as cyclic plastic-zone sizes will generally not exceed a few micrometers, and the crack sizes relevant to the HCF problem are invariably larger than the characteristic microstructural dimensions.

In the present work, the near-threshold crack-growth rate behavior of large (>5 mm) cracks tested under both constant-R and constant-K_{max} conditions is evaluated. Large crack behavior is compared to propagation behavior of naturally-initiated small (~45–1000 μm) cracks, and small (<500 μm) surface cracks initiated from sites of simulated foreign object damage (FOD), (all evaluated in the same Ti-6Al-4V microstructure). Specifically, we examine whether "worst-case" threshold values, measured for large cracks, can have any utility as a *practical* lower bound for the onset of small-crack growth under HCF conditions. The high load ratio large-crack tests are believed to eliminate the crack closure mechanism, thereby simulating the behavior of small cracks that are larger than microstructural dimensions but do not have a developed wake.

EXPERIMENTAL PROCEDURES

A Ti-6Al-4V alloy (6.30Al, 4.17V, 0.19Fe, 0.19O, 0.13N, bal. Ti (wt%)) was supplied as 20 mm thick forged plates from Teledyne Titanium after solution treating 1 hr at 925°C and vacuum annealing for 2 hr at 700°C. The microstructure consisted of a bimodal distribution of ~60 vol% primary-α and ~40 vol% lamellar colonies of $\alpha+\beta$, with a UTS of 970 MPa, a yield strength of 930 MPa and a Young's modulus of 116 GPa [9]. To minimize residual machining stresses, all samples were subsequently low-stress ground and chemically milled to remove ~30–100 µm of material.

Large-crack propagation studies were conducted on compact-tension C(T) specimens (L-T orientation; 8 mm thick, 25 mm wide) at R ratios (ratio of minimum to maximum loads) varying from 0.10 to 0.96 in a lab air environment (22°C, ~45% relative humidity). Crack lengths were monitored *in situ* using back-face strain compliance and verified periodically by optical inspection. Crack closure was also monitored using back-face strain compliance; specifically, the (global) closure stress intensity, K_{cl}, was approximated from the closure load, P_{cl}, measured at the point of first deviation from linearity in the elastic compliance curve upon unloading. Based on such measurements, an effective (near-tip) stress-intensity range, $\Delta K_{eff} = K_{max} - K_{cl}$, was determined. To approach the threshold, both constant-R and constant-K_{max} loading regimens were employed. Under both conditions, loads were shed with the normalized K-gradient of -0.08 mm^{-1} as suggested in ASTM E647. The constant-K_{max} tests were used to achieve threshold values at very high load ratios to minimize the effects of closure and represent worst-case *in-service* load ratios [10,11]. At 50-200 Hz (sine wave), tests were conducted on servo-hydraulic testing machines operating under automated closed-loop K control, with the fatigue thresholds, ΔK_{TH} and $K_{max,TH}$, defined as the minimum values of these parameters at a propagation rate of 10^{-10} m/cycle. Corresponding fatigue tests at 1000 Hz were performed under K control on a newly developed MTS servohydraulic test frame using a voice-coil servovalve.

RESULTS AND DISCUSSION

Effect of frequency: A comparison of fatigue crack growth behavior at 50 Hz and 1000 Hz is shown in Fig. 1. Cursory experiments at 200 Hz lie within the scatter of the 50 Hz and 1000 Hz data indicating that near-threshold behavior is essentially frequency independent in the range of 50 Hz – 1000 Hz. The apparent lack of a significant frequency effect on near-threshold behavior has also been observed at 1.5 kHz [12], and 20,000 Hz [13] on the same material (Fig. 2). Such frequency-independent growth rates for Ti alloys tested in air have also been reported for 0.1–50 Hz [14,15]; the current work extends this observation to beyond 1000 Hz. This result is particularly interesting in light of the significant accelerating effect of ambient air on fatigue crack growth when compared to behavior in vacuum. Davidson has shown that growth rates in vacuum (10^{-6} torr) are ~2 orders of magnitude slower than in air at an equivalent ΔK, although the non-propagation threshold remains roughly the same. This apparent discrepancy may be due to a environmental mechanism that is not rate-limited in the regime of 50-20,000 Hz. One suggested mechanism involves slip-step oxidation [16]: in air, as the loading cycle is applied, a freshly exposed slip-step oxidizes rapidly thereby preventing slip reversal during unloading. Based on the kinetic calculations of Gao, Simmons, and Wei [17], a freshly exposed slip-step would take ~1 minute to oxidize in a vacuum of 10^{-6} torr whereas in air the same oxidation process occurs in ~100 ns. For this reason, the behavior observed in vacuum would not be seen in air at any frequency < 10 MHz!

Effect of load ratio: Constant-R fatigue crack propagation is shown in Fig. 3 at four load ratios: R = 0.1, 0.3, 0.5, and 0.8 (50 Hz). These results are compared to constant-K_{max} fatigue crack propagation at four K_{max} values: K_{max} = 26.5, 36.5, 46.5, and 56.5 MPa$\sqrt{m}$ (1000 Hz). As expected, higher load ratios induce lower ΔK_{th} thresholds and faster growth rates at a given applied ΔK. The role of load ratio is commonly attributed to crack closure, which in Ti alloys is mainly associated with roughness-induced closure [18-20]. Based on compliance measurements, no closure was detected above $R = 0.5$; however, at $R = 0.1$-0.3, K_{cl} values were roughly constant at ~2.0 MPa√m. The measured variation of ΔK_{th} and $K_{max,th}$ values with R are compared in Figs. 5a and 5b. As originally suggested by Schmidt and Paris [21], if the load required to induce closure is independent of load ratio; and, if the variation in threshold with load ratio is simply due to the presence of closure, one would expect a transition in behavior from a K_{max}-invariant threshold at low R to a ΔK-invariant threshold at high R. The transition would be expected to occur at the load ratio where $K_{min,th} = K_{cl}$. The present results are consistent with this analysis and provide an indirect verification that $K_{cl} \sim 2$ MPa√m. This closure level is further supported by the observation that $R = 0.3$ and $R = 0.5$ growth-rate data merge at $\Delta K > 4.7$ MPa√m (where the $R = 0.3$ behavior is closure-free since $K_{min,R=0.3} > 2$ MPa√m). Perhaps the most convincing presentation of this transition from a closure-influenced- to a closure-free-threshold is shown in a plot of ΔK_{th} versus $K_{max,th}$ (Fig. 5c, which is simply a coordinate transformation of Figs. 5a and 5b).

Correcting for closure by characterizing growth in terms of ΔK_{eff} collapses the low load ratio data (R < 0.5) onto a single curve, Fig. 6 [see also 22]. However, above $R \sim 0.5$ where closure is presumed to be eliminated, ΔK_{TH} values continue to decrease with increasing R. This is observable in the ΔK_{th}-$K_{max,th}$ behavior as well (Fig. 5c): in the region where threshold is K_{max}-controlled, ΔK_{th} is not invariant and continues to drop with increasing K_{max}. This indicates that above $R \sim 0.5$, alternative K_{max}-controlled mechanisms may cause the load ratio effect. This mechanism is most likely related to the Marci effect observed in Ti-6Al-2Sn-4Zr-6Mo as well as other alloys [23] where, above a certain K_{max} condition, crack growth rates no longer diminish as ΔK is shed, and cracks can propagate at all applied ΔK levels.

There have been several proposed explanations for this observed K_{max} influence on thresholds at very high load ratios. These are described briefly below:

(a) Room temperature creep crack growth. Significant room temperature creep has been observed in Ti-6Al-4V when the applied stress is > ~80% of the yield strength and has been used to analyze the effect of load ratio on S/N behavior [24].

(b) Near-tip closure. Recent *in situ* SEM studies on the mechanisms for fatigue crack propagation in Ti-6Al-4V [12] have indicated that even at very high load ratios (R~0.8), there may be significant crack wake interference (closure) up to ~100 μm behind the crack tip. While this near-tip closure would not be detectable by standard closure measurements (i.e. compliance-based measurements), it could significantly shield the crack-tip from fully unloading.

(c) Stress-assisted hydride formation. Several independent studies have concluded that under sufficient triaxial stress, internal hydrogen can precipitate as metal hydrides (specifically, TiH_2) at α/β [25] or α/α [26] interfaces leading to brittle fracture along the interface. This phenomena has been used to explain both sustained load cracking [27,28] where crack advance is observed under monotonic load and accelerated fatigue crack growth at high load ratios [25,29]. Pao, Feng and Gill [25] have shown that, at a constant load ratio ($R = 0.9$), the near-threshold fatigue behavior is dependent on the internal hydrogen content, with threshold values dropping from 2.7 MPa√m (at 40 ppm H) to 2.0 MPa√m (at 1000 ppm H) Fig. 7. The influence of internal hydrogen content on fatigue crack propagation is distinctly similar to the influence of K_{max}.

In distinguishing which of the above mechanisms is responsible for this "additional" load-ratio effect, perhaps the most insightful observations are related to sustained load cracking (SLC). Several investigators have shown that when K is sufficiently high, cracks can grow under monotonic loading in Ti alloys [25-27]. Pao and O'Neal have observed the effect of internal hydrogen on SLC in Ti-6Al-2Sn-4Zr-6Mo and have distinguished it from creep which becomes a dominant mechanism above 720K. Boyer and Spurr have also studied SLC behavior and its relation to internal hydrogen content in Ti-6Al-4V, although they have shown that macroscopic SLC (>1 mm) is only operative below 273K when the hydrogen content is lower than ~200 ppm. However, in the current study SLC was observed at room temperature, although the crack growth was <100 μm prior to crack arrest, Fig 8. The observed microscopic SLC behavior may be at least partially responsible for the "additional" load ratio effect; however, it is likely that this effect is also related to the vastly different degrees of crack-tip plasticity.

Worst-case threshold concept: The problem of turbine engine HCF requires that design must be based on the notion of a threshold for no crack growth under conditions of high mean loads, ultrahigh frequencies and small crack sizes. Since the measurement of small-crack thresholds is experimentally tedious, the approach used here has been to simulate the mechanistic origins of the small-crack effect using "worst-case" large cracks, i.e., the measurement of thresholds under conditions which simulate the similitude limitation of small cracks by minimizing closure. To verify this "worst case" approach, the high load-ratio fatigue crack propagation data are compared to fatigue behavior from naturally initiated small cracks (~45–1000 μm) and small cracks (<500 μm) emanating from sites of foreign object damage; in both cases crack growth is not observed below ΔK ~ 2.9 MPa√m, Fig. 8 (details described in [30]). The present results show that with constant-K_{max} cycling at 1 kHz, a "worst-case" threshold can be defined in Ti-6Al-4V at ΔK_{TH} = 1.9 MPa√m (R ~ 0.95). Consequently, it is believed that the "worst-case" threshold concept can be used as a *practical* lower bound for the stress intensity required for the onset of small-crack growth under HCF conditions.

CONCLUSIONS

Based on an investigation into the high-cycle fatigue of a Ti-6Al-4V turbine engine alloy tested in air and vacuum at room temperatures, the following conclusions can be made:

1. Room temperature fatigue-crack growth (~10^{-12} to 10^{-6} m/cycle) and threshold ΔK_{TH} values were found to be frequency-independent over the range 50 to 1,000 Hz. Comparison to recent studies at 1500 Hz and 20,000 Hz as well as literature in the range of 0.1–50 Hz suggests that near-threshold behavior is frequency independent over 5 orders of magnitude.

2. Fatigue-crack growth rates *in vacuo* (~10^{-12} to 10^{-9} m/cycle) were ~2 orders of magnitude slower than corresponding rates in room air; ΔK_{TH} values, conversely, were unchanged. The apparent change in growth mechanism may be attributable to a mechanism such as slip-step oxidation where the rate of the reaction is faster than the cycle time over the range of frequencies studied.

3. The influence of load ratio is only partially explained by the closure mechanism. An additional mechanism causes thresholds to decrease below the "closure-free" threshold as R or, K_{max}) is increased. Observations of sustained load cracking indicate that this mechanism is most likely related to stress-induced hydride formation.

4. A "worst-case" fatigue threshold, measured for large cracks at R = 0.95 under constant-K_{max} conditions, was found to be 1.9 MPa√m for this alloy. This should be compared with measurements on naturally-initiated small cracks and FOD-initiated small cracks in the same microstructure, where small-crack growth was not reported below ΔK ~ 2.9 MPa√m. The long-crack K_{max} method is considered to provide a *practical* lower bound to design against the onset of growth of small cracks (when the small cracks are larger than microstructural dimensions).

Acknowledgments: Supported by the Air Force Office of Scientific Research by the Multidisciplinary University Research Initiative on *High Cycle Fatigue* to the University of California under Grant No. F49620-96-1-0478. We thank the Hertz Foundation (for supporting B.L.B.), Drs. G. Lütjering, J. A. Hines and J. O. Peters for their small-crack data, Dr. D.L. Davidson for his *in vacuo* data, and Dr. A.W. Thompson for helpful discussion.

REFERENCES

1. Report of the *Ad Hoc* Committee on Air Force Aircraft Jet Engine Manufacturing and Production Processes (1992). USAF Scientific Advisory Board, Pentagon, Washington, D.C.
2. B. A. Cowles (1996) *Int. J. Fract.* **80**, 147.
3. J. C. I. Chang (1996) An integrated research approach to attack engine HCF problems. Air Force Office of Scientific Research, Bolling AFB, Washington, D.C.
4. D. Taylor (1985) *A Compendium of Fatigue Thresholds and Crack Growth Rates*. EMAS Ltd., Warley, U.K.
5. J. K. Gregory (1994) in *Handbook of Fatigue Crack Propagation in Metallic Structures* (Edited by A. Carpinteri), Elsevier, Science, p. 281.
6. J. M. Larsen, B. D. Worth, C. G. Annis, and F. K. Haake (1996) *Int. J. Fract.* **80**, 237.
7. R. O. Ritchie (1996) in *Proceedings of the ASME Aerospace Division*, J. C. I. Chang, J. Coulter, *et al.*, eds., ASME, New York, NY, AMD Vol. 52, pp. 321.
8. R. O. Ritchie and J. Lankford (1986) *Mater. Sci. Eng.* **84**, 11.
9. D. Eylon (1998) Summary of the available information on the processing of the Ti-6Al-4V HCF/LCF program plates. University of Dayton Report, Dayton, OH.
10. H. Döker, V. Bachmann and G. Marci (1982) in *Fatigue Thresholds*, Proc. 1st Intl. Conf., J. Bäcklund, A. F. Blom and C. J. Beevers, eds., EMAS Ltd., Warley, U.K., vol. 1, p. 45.
11. W. A. Herman, R. W. Hertzberg, R. Jaccard (1988) *Fat. Fract. Eng. Mater. Struct.* **11**, 303.
12. D. Davidson, AFOSR Report, Southwest Research Institute, July 1998.
13. H. R. Mayer and S. E. Stanzl-Tschegg, Universität für Bodenkultur, Private Communication, 1998.
14. R. J. H. Wanhill (1974) *Corrosion-NACE* **30**, 28.
15. D. B. Dawson and R. M. N. Pelloux (1974) *Metall. Trans.* **5**, 723.
16. M. Sugano, S. Kanno, and T. Satake (1989) *Acta Metall.* **37**, 1811.
17. S. J. Gao, G. W. Simmons, and R. P. Wei (1984) *Mater. Sci. Eng.* **62**, 65.
18. M. D. Halliday and C. J. Beevers (1981) *J. Test. Eval.* **9**(4), 195.
19. K. S. Ravichandran (1991) *Acta Metall. Mater.* **39**(3), 401.
20. T. Ogawa, K. Tokaji, and K. Ohya (1993) *Fat. Fract. Eng. Mater. Struct.* **16**(9), 973.
21. R. A. Schmidt and P. C. Paris (1973) in *Progress in Fatigue Crack Growth and Fracture Testing*. ASTM STP 536, p. 79.
22. S. Dubey, A. B. O. Soboyejo, and W. O. Soboyejo (1997) *Acta Mater.* **45**(7), 2777.
23. M. Lang, G. A. Hartman, and J. M. Larsen (1998) *Scripta Mater.* **38**(12), 1803.
24. R. J. Morrissey, D. L. McDowell, and T. Nicholas, (1998) in *Proc. 3rd National Turbine Engine High Cycle Fatigue Conf.*, W. A. Stange and J. Henderson, eds., Universal Technology Corp., Dayton, OH, CD-Rom, session 10, p. 6.
25. P. S. Pao, C. R. Feng, and S. J. Gill (1998) *Scripta Mater.*, **40**(1), 19.
26. K. A. Peterson, J. C. Schwanebeck, and W. W. Gerberich (1978) *Met. Trans. A*, **9A**, 1169.
27. S. M. Sastry, R. J. Lederich, and B. B. Rath (1981) *Met. Trans. A*, **12A**, 83.
28. R. R. Boyer and W. F. Spurr (1978) *Met. Trans. A*, **9A**, 23.
29. P. S. Pao and J. E. O'Neal (1984) *J. Nuc. Mater.*, **122&123**, 1587.
30. B. L. Boyce, J. P. Campbell, O. Roder, A. W. Thompson, W. W. Milligan, and R. O. Ritchie (1999) *Int. J. Fatigue*, In Press.
31. J. A. Hines, J. O. Peters, and G. Lütjering, Technische Universität Hamburg-Harburg, Private Communication (1998).

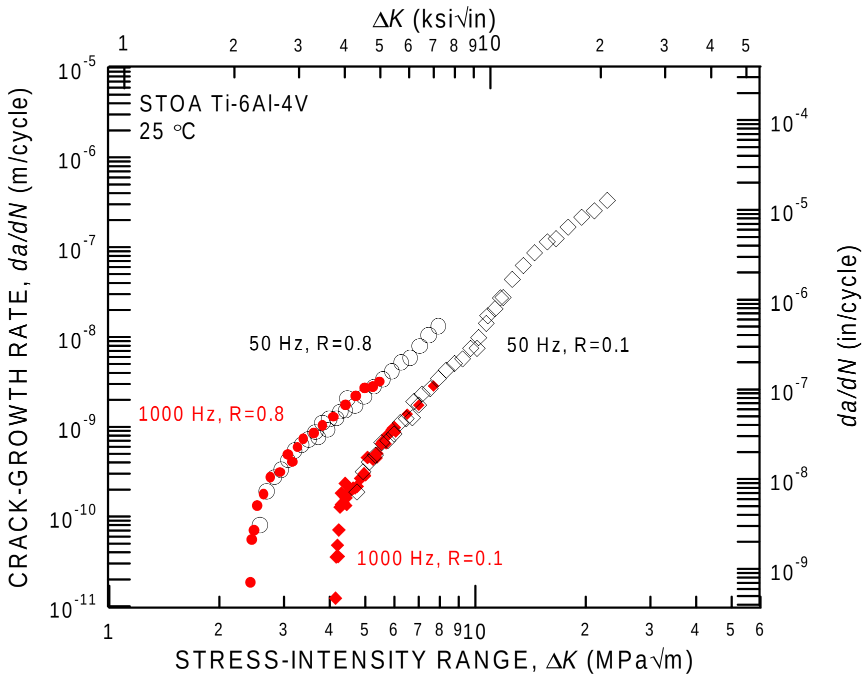

Figure 1. The effect of frequency on fatigue crack propagation. 50 Hz and 1000 Hz data was collected at $R = 0.1$ and $R = 0.8$. Cursory experiments at 200 Hz were coincident with the 50 Hz and 1000 Hz behavior, indicating that there is no significant effect of frequency in the range of 50-1000 Hz.

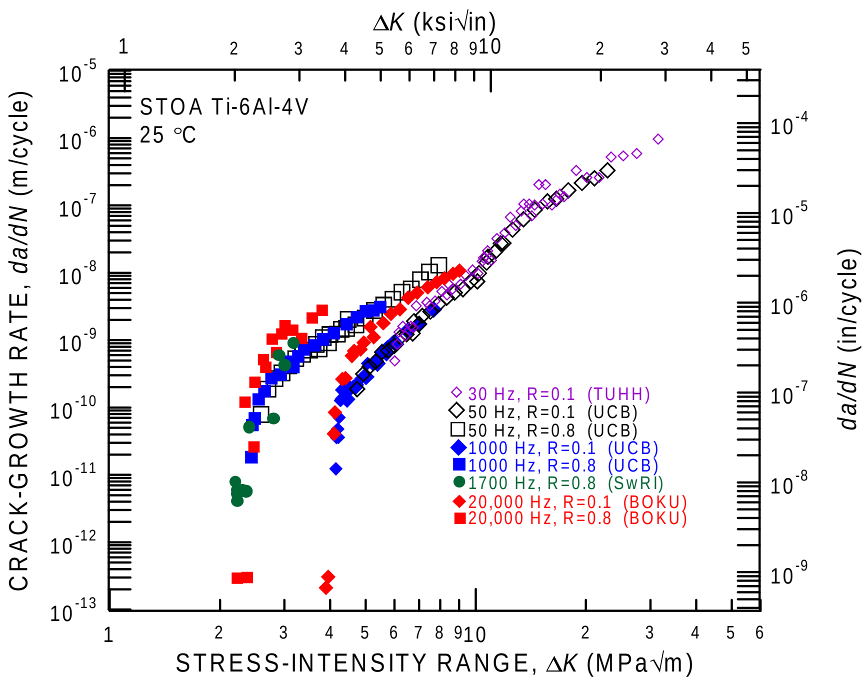

Figure 2. Results shown in Figure 1 compared to results on the same material at 30 Hz collected by Hines, Peters, and Lütjering [31] (TUHH = Technische Universität Hamburg-Harburg), 1500 Hz collected by Davidson [12] (SwRI. = Southwest Research Institute), and 20,000 Hz collected by Mayer and Stanzl-Tschegg [13] (BOKU = Universität für Bodenkultur). While there may be a slight shift in the Paris regime between 1000 Hz and 20,000 Hz, near-threshold behavior appears to be unaffected by frequency.

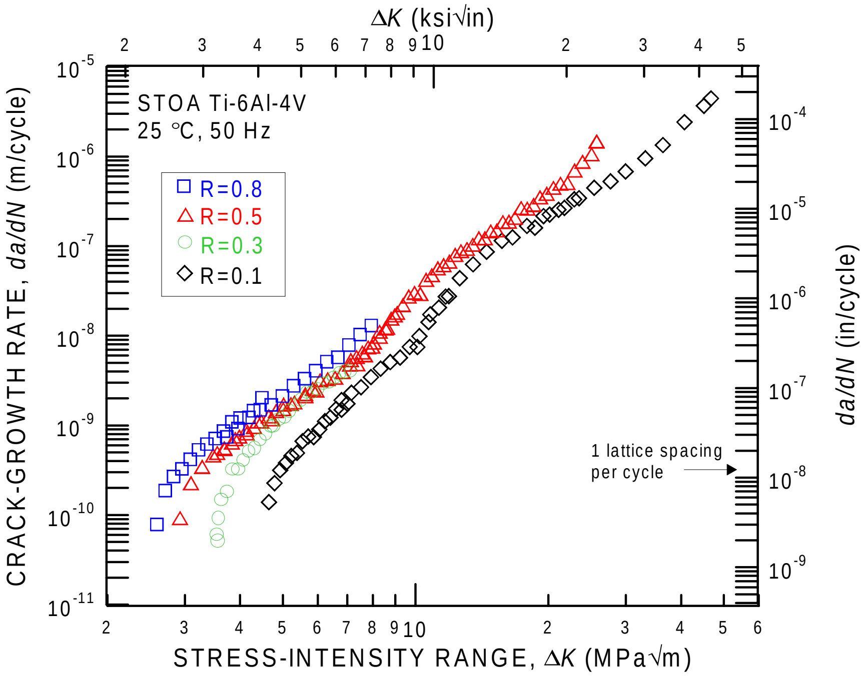

Figure 3. Constant-R fatigue crack propagation behavior at four different load ratios: R = 0.1, 0.3, 0.5, and 0.8 (50 Hz). Note that the R = 0.3 and 0.5 data merge at ΔK > 4.7 MPa√m.

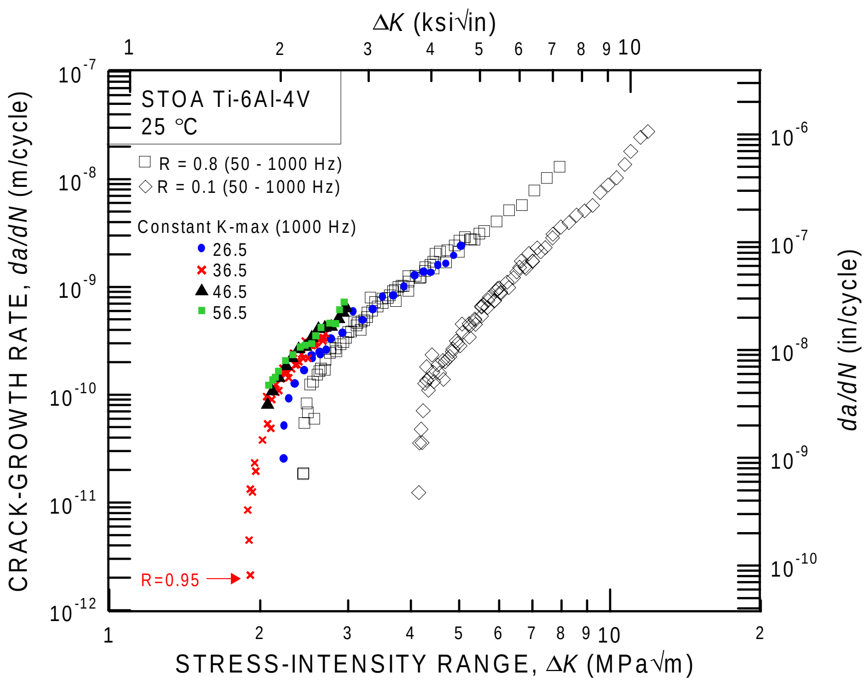

Figure 4. Constant-K_{max} fatigue crack propagation behavior at four different K_{max} values: K_{max} = 26.5, 36.5, 46.5, and 56.5 MPa√m (1000 Hz) compared to constant-R data at R = 0.1 and 0.8 (50-1000 Hz).

(a)

(b)

(c)

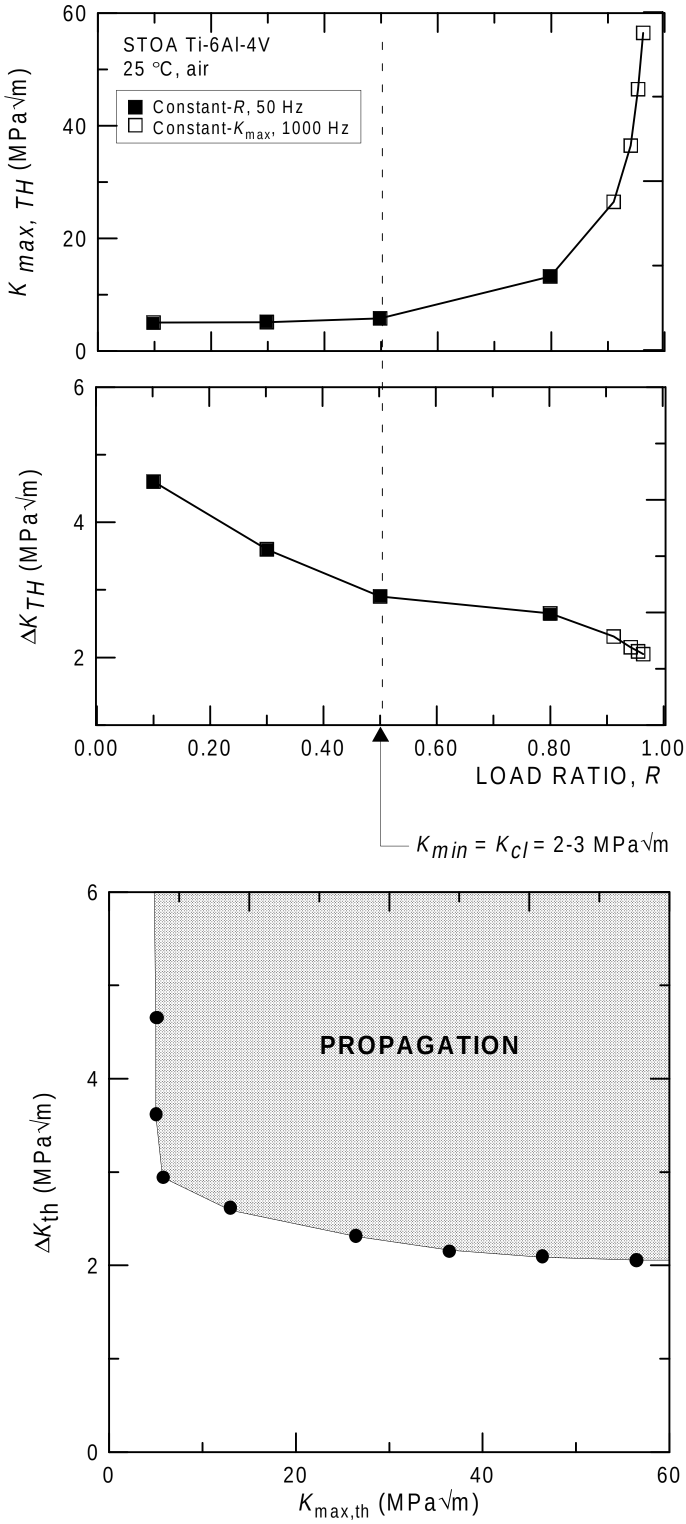

Figure 5. Combinations of (a) K_{max}-R, (b) ΔK-R, and (c) ΔK-K_{max} required for "threshold": growth at 10^{-10} m/cycle. As suggested by Schmidt and Paris [21], the closure mechanism would cause a transition from K_{max}-invariant growth to ΔK-invariant growth at the load ratio at which $K_{min} = K_{cl}$. This transition is most apparent in (c) where the threshold envelope changes from nearly vertical to nearly horizontal. The continued downward slope of the threshold envelope at high K_{max} values is presumably independent of closure.

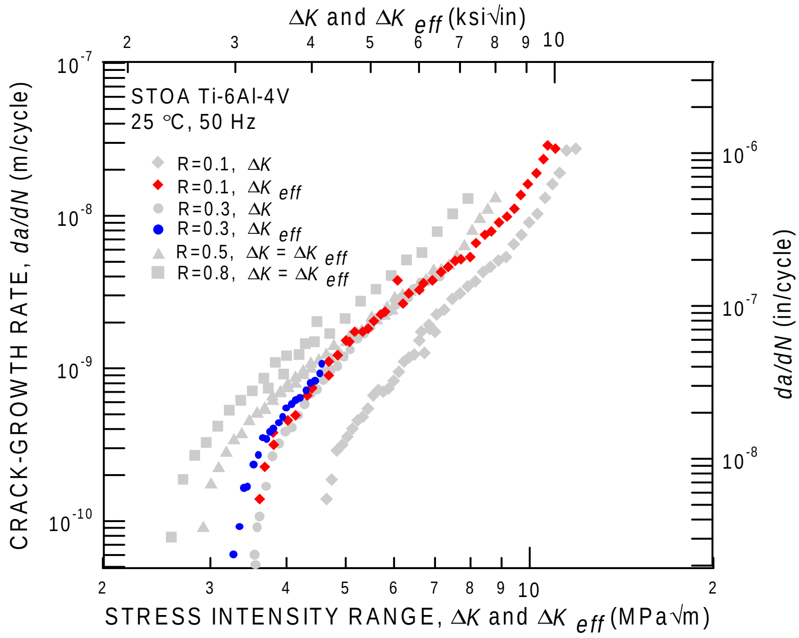

Figure 6. Correction for crack closure by characterizing growth rate in terms of ΔK_{eff} (= K_{max} – K_{cl}) collapses data at R < 0.5 onto a single curve. However, at R > 0.5, thresholds continue to drop, apparently in the absence of global closure.

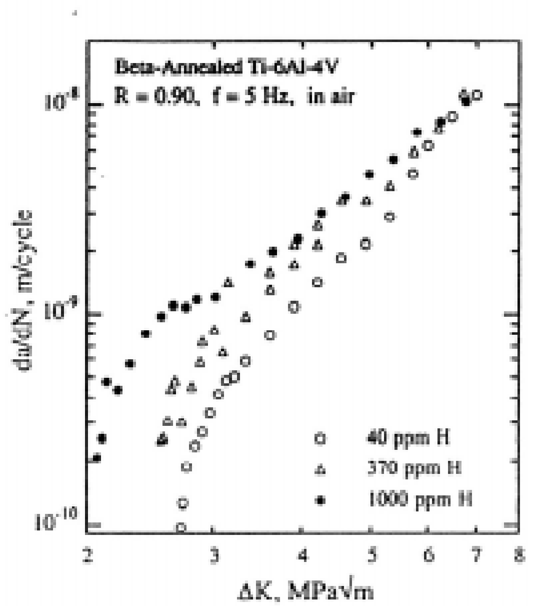

Figure 7. Fatigue crack propagation as affected by internal hydrogen content. From [25].

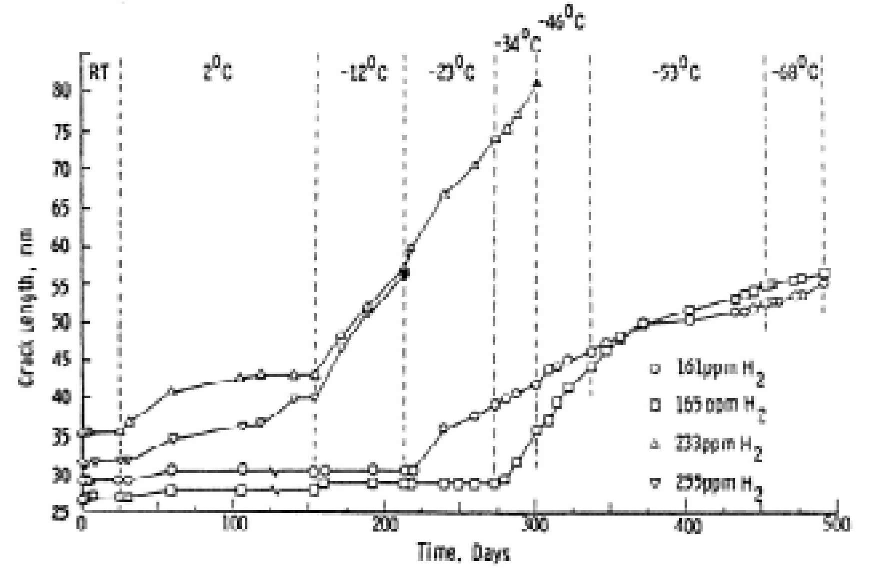

(a)

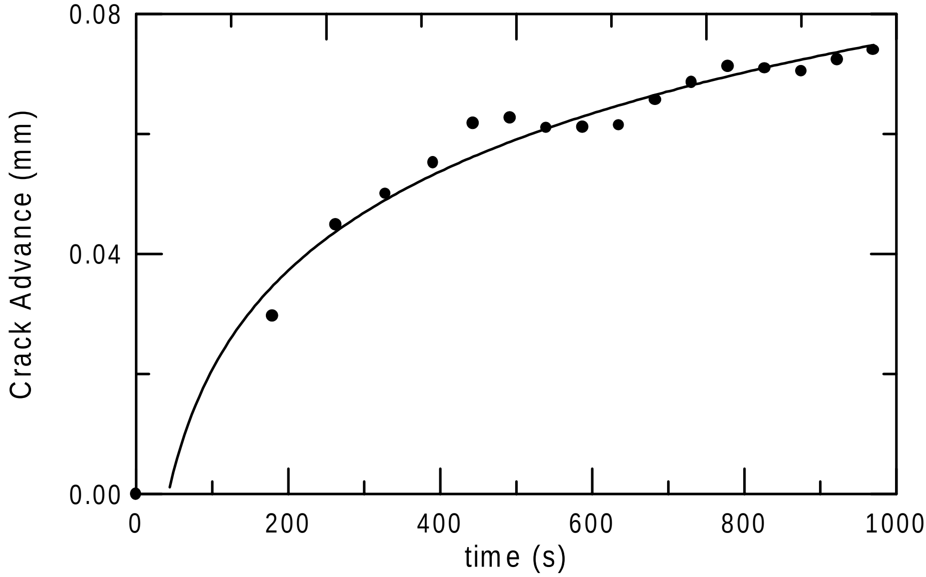

(b)

Figure 8. (a) An example of sustained load cracking (SLC) in Ti-6Al-4V where macroscopic growth (>1 mm) was observed at temperatures below 273K (0°C) [28]. (b) SLC observed in this study (at room temperature) was microscopic in that the crack propagated less than 100 μm before eventual arrest.

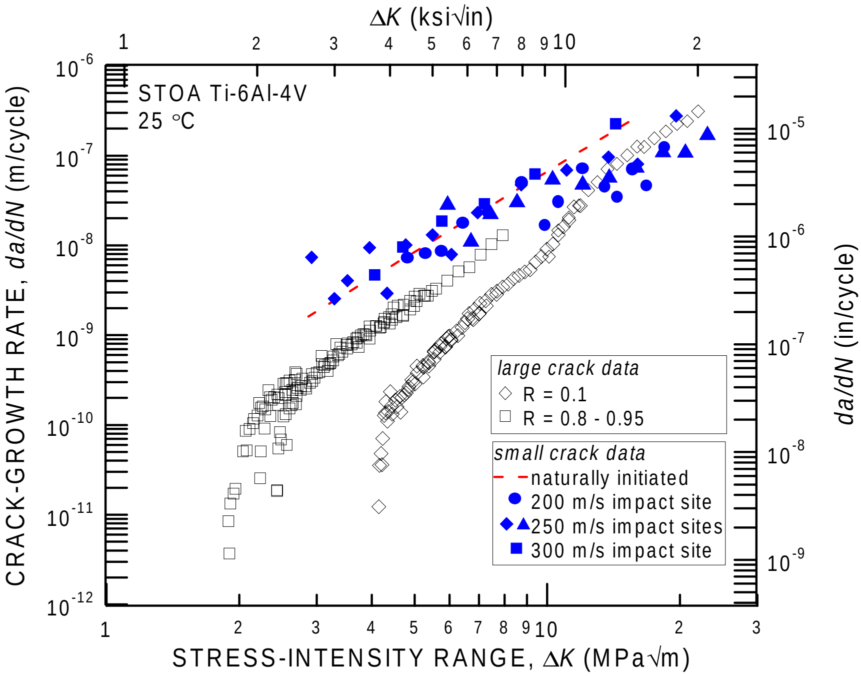

Figure 9. Comparison of long-crack propagation data to fatigue growth from naturally initiated small cracks and small cracks originating from sites of foreign object damage.

2/8/99 4:55 PM
Report No. UCB/R/98/

Department of Materials Science and Mineral Engineering
University of California at Berkeley

MIXED-MODE CRACK-GROWTH THRESHOLDS IN TI-6AL-4V UNDER TURBINE-ENGINE HIGH CYCLE FATIGUE LOADING CONDITIONS

J. P. Campbell, A. W. Thompson and R. O. Ritchie

Department of Materials Science and Mineral Engineering
University of California, Berkeley, CA 94720-1760

to be presented at the
4^{th} *National Turbine Engine High Cycle Fatigue Conference*
Monterey, California, Feb.1999

February 1999

Work supported by the U.S. Air Force Office of Scientific Research under Grant No. F49620-96-1-0478 under the auspices of the Multidisciplinary University Research Initiative on *High Cycle Fatigue* to the University of California.

Mixed-Mode Crack-Growth Thresholds in Ti-6Al-4V under Turbine-Engine High-Cycle Fatigue Loading Conditions

J.P. Campbell, A. W. Thompson and R. O. Ritchie
University of California, Berkeley
Department of Materials Science and Mineral Engineering
Berkeley, CA 94720-1760

Introduction

Multiaxial loading conditions are known to exist at fatigue-critical locations within turbine engine components, particularly in association with fretting fatigue in the blade-dovetail/ disk contact section [1]. Such stress states can result in fatigue-crack growth under the conjoint action of tensile and shear stresses. Under these conditions, commonly referred to as mixed-mode fatigue-crack growth, the resultant crack driving force is a combination of the influence of a mode I (tensile opening) stress intensity range, ΔK_I, as well as mode II (in-plane shear) and/or mode III (out-of-plane shear) stress intensity ranges, ΔK_{II} and ΔK_{III}, respectively.

While the vast majority of published and tabulated fatigue-crack growth data are measured for mode I loading only, it is well known that the superposition of shear loading can affect fatigue-crack growth resistance [2-10]. Specifically, the superposition of cyclic shear loading (ΔK_{II} or $\Delta K_{III} > 0$) to cyclic tensile opening of a crack has been generally observed to lower the value of ΔK_I at threshold. The necessity of quantifying this effect is clear in the case of high cycle fatigue of turbine-engine materials, where the extremely high cyclic loading frequencies ($v \sim 1 - 2$ kHz) and correspondingly short fatigue lives (in terms of *time* to failure) may require designing to the fatigue-crack growth threshold. Previous work by Pustejovsky suggests that a degradation in fatigue-crack growth resistance under the action of combined mode I/II loading is exhibited in Ti-6Al-4V [4,5]; however, mixed-mode fatigue-crack propagation data in Ti alloys are surprisingly scarce. Accordingly, the present paper describes initial efforts to map the mixed-mode fatigue-crack growth threshold envelope for mode I/ II loading in a bimodal microstructure of Ti-6Al-4V. Knowledge of such thresholds is essential for accurate prediction of the loading conditions under which fretting fatigue cracks will propagate until component failure. Specifically, such data have been identified as a critical input for the 'crack analogue' approach to fretting fatigue, which has been developed by Giannakopoulos *et al.* [11]. Although recent studies on fatigue-crack growth in single crystal Ni-based superalloys have raised the concern that the crack growth resistance may be severely degraded by mixed-mode loading conditions [12], the present results illustrate that the mixed-mode crack growth resistance of bimodal Ti-6Al-4V, quantified in terms of the range in strain energy release rate, ΔG, is in fact enhanced relative to that which is exhibited under pure mode I conditions.

Experimental procedure

Mixed-mode (I/II) crack-growth thresholds have been measured using the asymmetric four-point bend (AFPB) geometry, illustrated in Figure 1. The material investigated was taken from a solution treated and overaged forging of Ti-6Al-4V. This forging exhibited a bimodal microstructure (Figure 2), with approximately 60% primary α grains (~ 15 μm in diameter) in a lamellar $\alpha + \beta$ matrix. Bend bars with width and thickness of 11.3 mm and 4.5 mm, respectively, were cut in the L-T orientation by electrical discharge machining (EDM). The inner and outer loading spans (from load line to loading point) employed were 12.7 mm and 25.4 mm, respectively. Using this experimental geometry, mixed-mode loading conditions ranging from pure mode II to mode I dominant (i.e., a small value of $\Delta K_{II}/\Delta K_I$) may be achieved. Specific mixed-mode loading conditions, in terms of the ratio $\Delta K_{II}/\Delta K_I$, are accomplished by offsetting the crack from the load line, as suggested by the shear force and bending moment diagrams shown for the AFPB sample in Figure 1. In the present work, the mixed-mode loading conditions will be quantified both in terms of the ratio of ΔK_{II} to ΔK_I and the phase angle, β (= $\tan^{-1}(\Delta K_{II}/\Delta K_I)$). Pure mode I loading is characterized by $\Delta K_{II}/\Delta K_I = 0$ and $\beta = 0°$, while pure mode II is given by $\Delta K_{II}/\Delta K_I \rightarrow \infty$ and $\beta = 90°$.

Given the potentially strong influence of crack wake shielding effects [2,13-16], and hence precracking technique [7], on the measured crack growth behavior, a very specific precracking regimen was employed. Fatigue precracks were grown from a 2 mm deep EDM notch under pure mode I loading (using symmetric four-point bending) under computer automated stress intensity control with load ratio, $R = K_{min}/K_{max}$, of 0.1 and a cyclic loading frequency of 50 Hz (sine wave). Loads were shed at a K-gradient[1] of -0.15 such that a final precrack length of ~ 4.5 mm was achieved at a near-threshold ΔK of ~ 4.8 MPa√m. Following precracking, samples were loaded in AFPB with the fatigue precrack tip offset from the load line to achieve the desired phase angle. The necessary offset and the load levels required to achieved the desired magnitudes of ΔK_I and ΔK_{II} were determined using a recently updated version of the AFPB stress intensity solution by He and Hutchinson [17]. Samples were subjected to two million cycles at a frequency of 1000 Hz, after which the crack was inspected using an optical microscope to determine if growth had occurred. If no crack growth was observed, the value of ΔK_I or ΔK_{II} was increased by 0.25 MPa√m and the test repeated. In this way, the crack growth threshold was measured in terms of a "growth/no growth" combination of loading conditions bounding the true threshold for the onset of crack propagation. Using the methods described above, the threshold condition may be defined as crack growth rates less than 10^{-11} m/cycle. Tests have been conducted in air at R of 0.1, 0.5 and 0.8.

Results and Discussion

Mixed-mode threshold envelopes: Mixed-mode fatigue-crack growth threshold envelopes measured for $\Delta K_{II}/\Delta K_I$ ranging from zero (pure mode I, $\beta = 0°$) to approximately 2 ($\beta \sim 63°$) and R of 0.1, 0.5 and 0.8 are plotted in Figure 3, where crack growth thresholds are plotted as the mode II stress intensity range at threshold, ΔK_{II}, as a function of the corresponding value of the mode I stress intensity range at threshold, ΔK_I. The threshold envelope for each load ratio has been constructed as an interpolated curve. It is important to note that the measured thresholds are those for the onset of crack extension, which, for pure mode I loading, are known to be slightly higher than threshold

[1] The K-gradient, C, is defined such that $\Delta K_0 = \Delta K_i \exp(C(a_0 - a_i))$, where subscripts 0 and i refer to current and initial parameter values, respectively.

values determined by load shedding techniques [18,19]. In Figure 3, loading conditions characterized by combinations of ΔK_{II} and ΔK_I which lie outside the envelope (i.e., to the upper left with respect to the envelope curve) will result in crack propagation, while loading conditions lying inside the envelope will not produce crack extension. In all cases, crack propagation was observed to be deflected with respect to the precrack orientation; self-similar crack growth was not observed. In Figure 3, for b ~ 63° and R = 0.8, a single "no growth" data point is presented. For this particular loading condition, the loading limitation of the testing machine (5000 lb) was reached, but growth could not be induced.

Fatigue-crack growth resistance as a function of phase angle: Contrary to behavior reported for single-crystal Ni-based superalloys [12], where the value of ΔK_I at threshold was found to decrease with increasing amounts of superimposed shear loading (ΔK_{II}), the value of ΔK_I at threshold in Ti-6Al-4V is actually observed to increase slightly as $\Delta K_{II}/\Delta K_I$ is increased from 0 to 0.5 (β = 0° and ~ 26°, respectively) for all load ratios investigated (Figure 3). If $\Delta K_{II}/\Delta K_I$ is increased to 2 (β ~ 63°), the value of ΔK_I at threshold does decrease. This variation of ΔK_I at threshold with phase angle, β, is plotted in Figure 4a. However, using a single parameter characterization of the fatigue-crack growth resistance, ΔG, it is apparent that the fatigue-crack growth threshold (ΔG_{TH}), in fact, increases monotonically with phase angle, as shown in Figure 4b. For plane strain conditions, $\Delta G = (\Delta K_I^2 + \Delta K_{II}^2)(1- \nu^2)/E$. Young's modulus, E, and Poisson's ratio, ν, were taken to be, respectively, 0.3 and 116 MPa for the present calculations. Similar results have been reported for the case of monotonic crack growth resistance [20], where the mixed-mode fracture toughness, characterized by G, increases with the applied phase angle. Although further work is necessary to demonstrate the origin of this increase in crack growth resistance in the case of fatigue, it is believed to result in part from an enhancement of extrinsic crack tip shielding when the fatigue fracture surfaces are sheared with respect to one another [13]. Such shear displacement in the crack wake likely produces both frictional resistance and perhaps even asperity interlock which will shield the crack tip from the applied value of ΔK_{II}, as well as an increase in the level of traditional mode I crack closure (and hence shielding with respect to ΔK_I), as the registry of fracture surface asperities is decreased by the applied shear. It is also speculated that the slight increase in ΔK_I at threshold observed as β increase from 0 to ~ 26° (ΔK_{II}/ ΔK_I of 0 and 0.5, respectively) is associated with this enhancement of mode I closure; at β ~ 63° (ΔK_{II}/ ΔK_I ~ 2), the value of ΔK_I at threshold is believed to decrease due to the significantly higher driving force associated with the high value of ΔK_{II}.

Influence of load ratio: In Figure 3, it is apparent that, consistent with the widely recognized influence of load ratio on fatigue crack growth threshold for pure mode I loading, the mixed-mode crack growth threshold is degraded as load ratio increases. However, the crack growth threshold does not vary uniformly with load ratio for each phase angle investigated. This point is more clearly illustrated when the threshold condition for crack propagation under mixed-mode loading is expressed in terms of a single characterizing parameter. In Figure 5, the value of ΔG_{TH} is plotted as a function of load ratio, R, for each of the phase angles investigated (β ~ 0°, 26° and 63°). At each value of β, the crack growth threshold is observed to decrease with increasing R;

however, for each phase angle the dependence of ΔG_{TH} on β is slightly different. For pure mode I loading ($\Delta K_{II}/\Delta K_I = 0$), the fatigue crack growth threshold exhibits a well-documented transition from a region where the threshold is strongly dependent on R (for low values of R), to a region of significantly reduced load ratio dependence (at high R). This trend has been very clearly demonstrated by Boyce and Ritchie [21] for pure mode I fatigue-crack growth in the same bimodal Ti-6Al-4V. However, for $\Delta K_{II}/\Delta K_I \sim 0.5$ and 2, the dependence of ΔG_{TH} on R is different. For $\Delta K_{II}/\Delta K_I \sim 0.5$, ΔG_{TH} shows a relative strong dependence on R over the entire range of load ratio investigated; a region of reduced R dependence at higher load ratios, analogous to that observed for pure mode I loading, is not observed. For $\Delta K_{II}/\Delta K_I \sim 2$, however, the dependence of ΔG_{TH} on load ratio for low values of R (= 0.1 to 0.5) is substantially weaker than that exhibited for $\Delta K_{II}/\Delta K_I$ of 0 and 0.5 over the same range of R.

Conclusions

Based on a study of mixed-mode (I + II) fatigue-crack growth in bimodal Ti-6Al-4V, it is observed that the threshold for crack propagation (characterized in terms of ΔG), increases monotonically as the phase angle, β, is increased. Consequently, for the case fatigue-crack growth in bimodal Ti-6Al-4V, mixed-mode loading should not hamper the ability to design against crack propagation under HCF conditions, provided that mixed-mode stress states existing in actual turbine-engine components can be properly identified and analyzed. Additionally, it is found that the fatigue-crack growth threshold shows a complex dependence on load ratio and phase angle; the crack growth threshold is observed to decrease as load ratio increases for each phase angle, but the rate of decrease in threshold with increasing R is different for each value of β.

Acknowledgments

This work is supported by the U.S. Air Force Office of Scientific Research under Grant No. F49620-96-1-0478 under the auspices of the Multidisciplinary University Research Initiative on *High Cycle Fatigue* to the University of California.

References

1. Waterhouse, R.B. and T.C. Lindley, Fretting Fatigue, ESIS Publication No. 18. European Structural Integrity Society, Mechanical Engineering Publications Limited, London, 1994.
2. Gao, H., M.W. Brown, and K.J. Miller, "Mixed-mode fatigue thresholds", *Fatigue Engng. Mater. Struct.*, **5**, p. 1-17 (1982).
3. Gao, H., N. Alagok, M.W. Brown, and K.J. Miller, "Growth of fatigue cracks under combined mode I and mode II loads", in *Multiaxial Fatigue, ASTM STP 853*, eds. K.J. Miller and M.W. Brown, ASTM, Philadelphia, PA, p. 184-202 (1985).
4. Pustejovsky, M.A., "Fatigue crack propagation in titanium under general in-plane loading - I: experiments", *Eng. Fract. Mech.*, **11**, p. 9-15 (1979).
5. Pustejovsky, M.A., "Fatigue crack propagation in titanium under general in-plane loading - II: analysis", *Eng. Fract. Mech.*, **11**, p. 17-31 (1979).
6. Tanaka, K., "Fatigue crack propagation from a crack inclined to the cyclic tensile axis", *Eng. Fract. Mech.*, **6**, p. 493-507 (1974).

7. Tong, J., J.R. Yates, and M.W. Brown, "The influence of precracking techniques on fatigue crack growth thresholds under mixed mode I/II loading conditions", *Fatigue Fract. Engng. Mater. Struct.*, **17**, p. 1261-1269 (1994).
8. Tong, J., J.R. Yates, and M.W. Brown, "The significance of mean stress on the fatigue crack growth threshold for mixed mode I + II loading", *Fatigue Fract. Engng. Mater. Struct.*, **17**, p. 829-838 (1994).
9. Zheng, Y.S., Z.G. Wang, and S.H. Ai, "Mixed-mode I and II fatigue threshold and crack closure in dual-phase steels", *Metall. Mater. Trans. A,* **25A**, p. 1713-1723 (1994).
10. Iida, S. and A.S. Kobayashi, "Crack-propagation rate in 7075-T6 plates under cyclic tensile and transverse shear loading", *J. Bas. Engng.*, **91**, p. 764-769 (1969).
11. Giannakopoulos, A.E., T.C. Lindley, and S. Suresh, "Aspects of equivalence between contact mechanics and fracture mechanics: theoretical connections and a life-prediction methodology for fretting-fatigue", *Acta Materialia,* **46**, p. 2955-2968 (1998).
12. John, R., D. DeLuca, T. Nicholas, and J. Porter, "Near-threshold crack growth behavior of a single crystal Ni-bas superalloy subjected to mixed mode loading", in *Mixed-Mode Crack Behavior,* ASTM STP 1359, eds. K.J. Miller and D.L. McDowell, (1998).
13. Nayeb-Hashemi, H., F.A. McClintock, and R.O. Ritchie, "Effects of friction and high torque on fatigue crack propagation in mode III", *Metall. Trans. A,* **13A**, p. 2197-2204 (1982).
14. Smith, M.C. and R.A. Smith, "Toward an understanding of mode II fatigue crack growth", in *Basic Questions in Fatigue*, Volume I, ASTM STP 924, eds. J.T. Fong and R.J. Fields, ASTM; Philadelphia, PA, p. 260-280 (1988).
15. Tong, J., J.R. Yates, and M.W. Brown, "A model for sliding mode crack closure. I: theory for pure mode II loading", *Eng. Fract. Mech.*, **52**, p. 599-611 (1995).
16. Tong, J., J.R. Yates, and M.W. Brown, "A model for sliding mode crack closure. II: mixed mode I and II loading and application", *Eng. Fract. Mech.*, **52**, p. 613-623 (1995).
17. He, M.Y. and J.W. Hutchinson, *MURI on High Cycle Fatigue,* unpublished research (1999).
18. Lenets, Y.N. and T. Nicholas, "Load history dependence of fatigue crack growth thresholds for a Ti-alloy", *Eng. Fract. Mech.,* **60**, p. 187-203 (1998).
19. Campbell, J.P., *MURI on High Cycle Fatigue,* unpublished research (1999).
20. Liu, C., M.L. Lovato, and M.G. Stout, "Measurement of the fracture toughness of a fiber-reinforced composite using the Brazilian disk geometry", *Int. J. Fract.,* **87**, p. 241-263 (1997).
21. Boyce, B.L. and R.O. Ritchie, "On the definition of lower-bound fatigue-crack propagation thresholds in Ti-6Al-4V under high cycle fatigue conditions", in *Proceedings of the 4th International Conference on High Cycle Fatigue*, (1999).

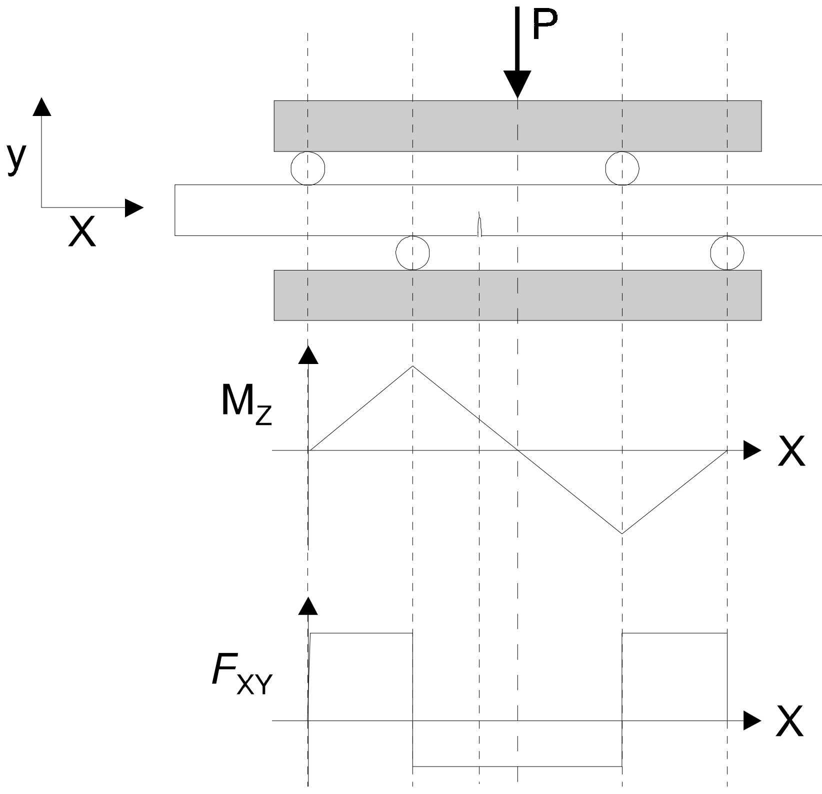

Figure 1: Schematic representation of the asymmetric four-point bend (AFPB) loading geometry. Shear force, F_{xy}, and bending moment, M_z, diagrams illustrate the capability of achieving a variety of mixed-mode loading conditions by offsetting the crack from the load line.

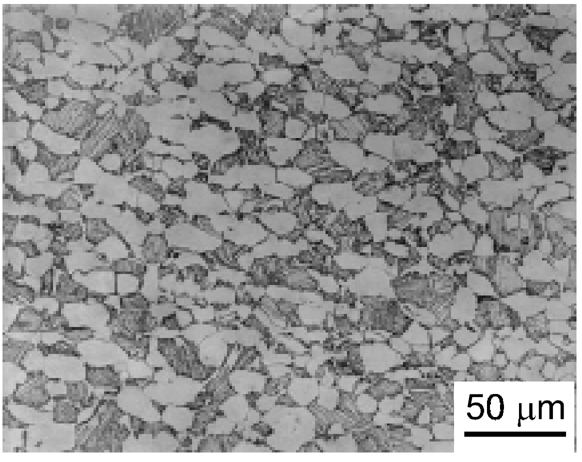

Figure 2: Optical photomicrograph of bimodal Ti-6Al-4V. The microstructure is characterized by ~ 60% primary α (grain diameter ~ 15 μm) in a matrix of lamellar α + β.

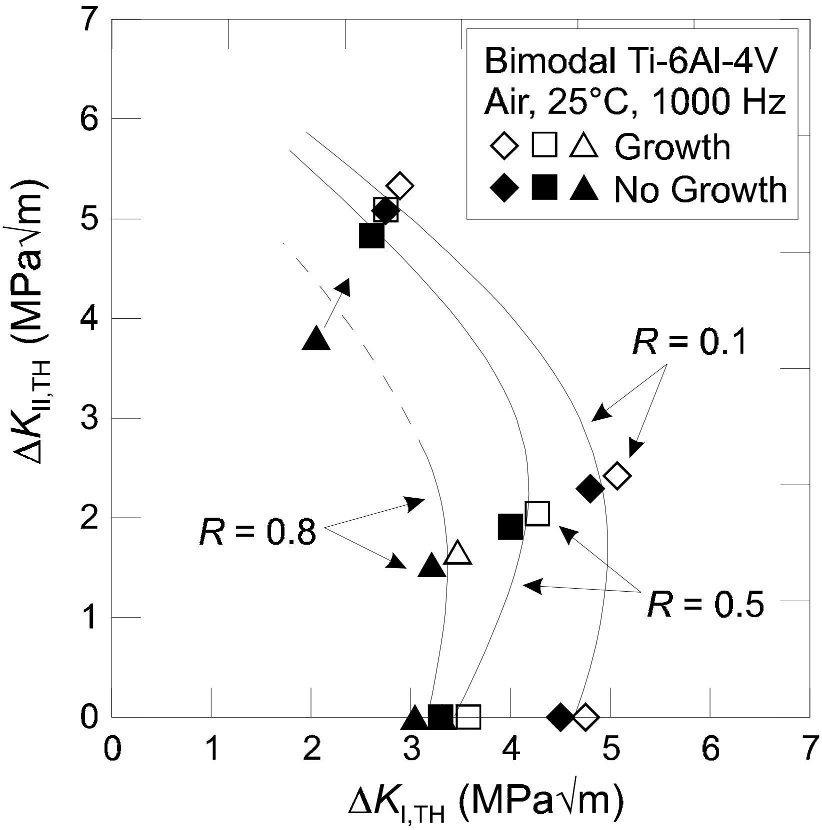

Figure 3: Mixed-mode fatigue-crack growth threshold envelopes for bimodal Ti-6Al-4V at load ratios, *R*, of 0.1, 0.5 and 0.8 and a cyclic loading frequency of 1000 Hz. The mode II stress intensity range at threshold, $\Delta K_{II,TH}$, is plotted as a function of the mode I stress intensity range at threshold, $\Delta K_{I,TH}$. Closed and open symbols represent the loading conditions that produced, respectively, no crack growth and crack growth. Thus, the true threshold for the onset of crack extension is bounded by the growth/ no growth combination of loading conditions.

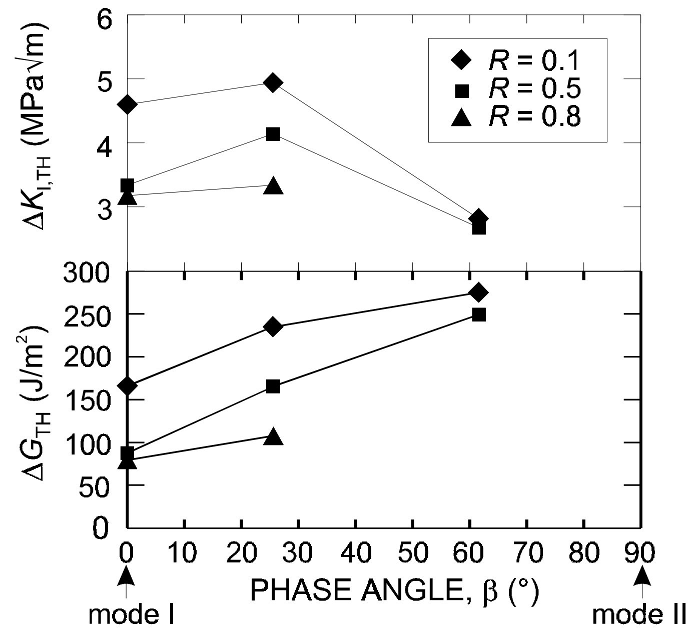

Figure 4: (a) The mode I stress intensity range at threshold, $\Delta K_{I,TH}$, is plotted as a function of the applied phase angle, β, for load ratios of 0.1, 0.5, and 0.8. $\Delta K_{I,TH}$ is observed to increase slightly as β increase from 0° to ~ 26° and then decrease for β ~ 63°. (b) The same mixed-mode fatigue crack growth thresholds are plotted in terms of the range in strain energy release rate at threshold, ΔG_{TH}, as a function of β. The fatigue-crack growth resistance at threshold is observed to increase with phase angle.

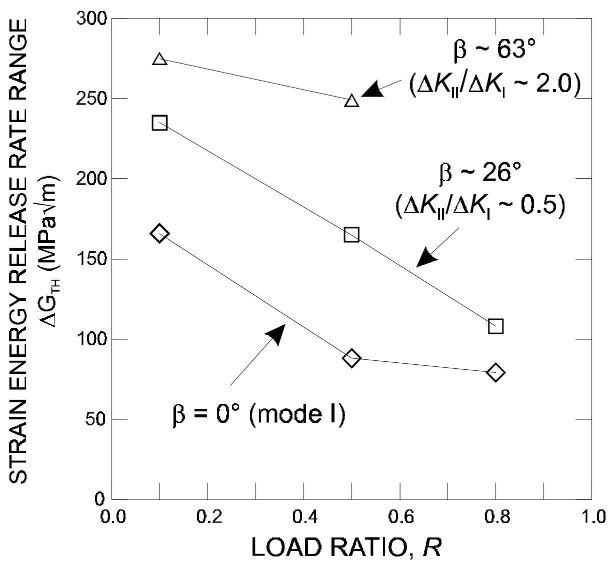

Figure 5: The range in strain energy release rate at threshold, ΔG_{TH}, is plotted as a function of load ratio, R, for β of 0°, 26° and 63°. For each phase angle investigate, ΔG_{TH} decreases with increasing R, however, the rated of decrease in the threshold appears to be a function of β.

Subcritical Crack Growth of Ti-6Al-4V in the Ripple-Loading Regime

Dr. James P. Thomas
University of Notre Dame
Department of Aerospace and Mechanical Engineering
Notre Dame, IN 46556-5637

Introduction

A number of recent failures of two-phase $\alpha + \beta$ titanium alloy fan and compressor components in commercial and military gas turbine engines have been attributed to high cycle fatigue (HCF) [1,2]. The problem involves crack initiation and propagation from various fretting, foreign-object-damage, etc. sites on rotating turbine components, which are subjected to high stress-ratio "ripple" loading. One goal of the current research on this problem is to significantly reduce HCF related maintenance costs through the development of a damage-tolerant design methodology [3]. Achievement of this goal requires better understanding of subcritical crack growth of these alloys under the influence of high stress-ratio (R) loading under the various service conditions.

Ti-6Al-4V is a two-phase titanium alloy commonly used for turbine fan and compressor components. The crack growth behavior of Ti-6Al-4V at stress ratio values less than 0.7 and the role of various material, mechanical, and environmental factors have been investigated [4,5,6,7,8]. This alloy is also known to be susceptible to sustained loading cracking (SLC) in air with hydrogen assisted cracking [7,8,9] and/or low temperature creep [6,10,11] as the most often suggested mechanisms. However, little information is available on high R-ratio crack growth of Ti-6Al-4V and the role played by SLC during fatigue.

To gain a better understanding of high stress-ratio ($R \geq 0.9$) cracking of this alloy, fatigue and SLC experiments were conducted at temperatures ranging from –30 to 140 $^{\circ}C$. This paper reports fatigue crack growth rates (CGR) as a function of stress intensity and temperature; SLC data; and optical and scanning electron fractography. The test results show that temperature had little affect on fatigue crack growth. Transient crack growth followed by crack arrest was observed under sustained load conditions. A significant increase in crack tunneling occurred as the temperature was decreased suggesting a hydrogen related cracking mechanism. Recommendations for additional tests with thicker or side-grooved specimens and with different hydrogen levels are made.

Material and Experimental Procedures

Mini-compact tension C(T) specimens with $W = 20mm$ and $B = 4.9mm$ were machined from the Ti-6Al-4V plate forging in the L-T orientation. The material was forged at 1720°*F* (938°*C*), 106°*C* below β-transus, solution-treated in air at 1710°*F* (932°*C*) for 75 minutes, air cooled, then vacuum annealed at 1300°*F* $\pm 25°C$ (704°*F*) and 5×10^{-7} torr for 2 hours followed by fan cooling in an Argon atmosphere (AMS 4928) [12]. The microstructure is roughly equiaxed with approximately 57% α and 43% Widmanstätten $\alpha+\beta$ (Figure 1). Composition and mechanical properties for this material are reported in Tables 1 and 2.

The fatigue and SLC tests were conducted using an MTS servohydraulic test system with computer-automated control and data acquisition and an environmental chamber for temperature control. Constant *R*-ratio and constant $K_{\max}$ fatigue tests were conducted using the ASTM [13] *K* expression for C(T) specimens and the exponential relationship: $\Delta K = \Delta K_0 \exp[C(a-a_0)]$ with $C = \pm 0.08 mm^{-1}$. The SLC tests were conducted under load control with an initial $K_{\max} \approx 65$ and $60 MPa\sqrt{m}$. Fatigue cracking prior to the SLC tests was conducted at $K_{\max} = 15 MPa\sqrt{m}$ and *R*=0.1. Crack length was measured using a reversing current DC potential drop technique with an estimated crack length resolution of $5\,\mu m$ or better. Crack growth rates were computed using a seven-point-incremental-straight-line-fit of the post-test corrected crack-length/cycles data.

Results and Discussion

Fatigue CGR data for $R = 0.9$ at 22, 75 and $140^\circ C$ are shown in Figures 2 through 5. The influence of temperature is negligible in the range of test conditions considered. The combined data at all temperatures yield the threshold estimate: $\Delta K_{th} = 2.04 MPa\sqrt{m}$ corresponding to $da/dN = 10^{-7}\, mm/cycle$ and the Paris-law relationship:

$$\frac{da}{dN} = 2.17\times10^{-8}\,\Delta K^{3.36}$$

in the mid-range ΔK regime. The results are not particularly remarkable other than to note the relatively small degree of scatter in the data and the classical three-stage behavior exhibited by the CGR curves. The observed lack of influence of temperature on the fatigue CGR's is consistent with the studies mentioned in Rosenberg et al. [4] who report small or negligible temperature effects depending on microstructure, load ratio, and temperature range.

Fracture surfaces for the 22 and $140^\circ C$ tests at various ΔK levels are shown in Figures 7-12. The $22^\circ C$ fracture morphology exhibits cleavage facets ≈ 10 to $30\mu m$ in size and fine river marks on the faces and side ledges. Secondary cracking is also present along with a small number of void or cavity-like features. The low ΔK fracture surface is less "blocky" in appearance and exhibits fewer secondary cracks and voids giving it a slightly "smoother" appearance than the mid-level ΔK surface. The $140^\circ C$ morphology is also cleavage in nature but much less blocky in appearance, and there are also fewer secondary cracks and voids at the low ΔK levels.

A correlation between the fracture topography and the microstructure of Ti-6Al-4V in the solution-treated and over-aged condition (similar to the DA condition) has been described by Chesnutt et al. [5] and is relevant to the morphology exhibited in Figures 7 and 9:

> At low growth rates, it appears that fatigue crack propagation occurs by mixed modes consisting of striation formation, 'cleavage' of the primary α particles or at the primary α-Widmanstätten $\alpha+\beta$ interfaces, and/or 'cleavage' of the Widmanstätten $\alpha+\beta$ interfaces." and "Considerable secondary cracking at α-$\alpha+\beta$ interfaces and Widmanstätten $\alpha+\beta$ packet boundaries evidently occurs, especially at the intermediate growth rate.

No striations are visible on the fracture surfaces, and this consistent with models (e.g., [14]) which correlate striation formation with cyclic plastic zone sizes larger than the material grain size. The cyclic plastic zone size for $\Delta K \approx 4.0 MPa\sqrt{m}$ is $2r_{cpz} \approx 1.2\mu m$ [14], which is much smaller than the average grain size (cf. Figure 1).

Figure 6 shows the CGR data obtained under constant $K_{\max} = 60 MPa\sqrt{m}$, ΔK decreasing conditions ($R \approx 0.97$ at threshold). The influence of temperature in the range of 22 to$140^{\circ}C$ is negligible. The threshold value averaged over all temperatures is $\Delta K_{th} \approx 2.00 MPa\sqrt{m}$, which is approximately 2% lower than that observed in the constant-*R* tests. Fracture surfaces for $K_{\max}$ constant tests at 22 and $140^{\circ}C$ are shown in Figures 13 and 14. The $140^{\circ}C$ fracture surface shows a few more voids than the $22^{\circ}C$ surface, and both surfaces exhibit more voids and tear ridges than the constant-*R* fractures.

Constant $K_{\max}$-decreasing ΔK testing is used to determine an "intrinsic" threshold level that is unaffected by crack closure (e.g., [15]). Use of this procedure with certain titanium alloys has led to the discovery of an interesting phenomenon where the CGR increases as ΔK decreases below ΔK_{th} for $K_{\max}$ values above some limit [16,17]. This phenomenon is referred to as the "Marci effect", and speculations on its cause center on the presence of an increasing SLC-CGR component as ΔK decreases and the mean stress increases. The Marci effect has not been observed in the completed tests with this alloy.

The constant-load SLC tests exhibited transient CG at the start of the tests that eventually diminished in a matter of hours. Large dimples were formed at the crack tips on the sides of the specimens indicating the presence of significant plastic straining. Crack growth consisted primarily of tunneling, and the extent of tunneling depended strongly on the load and temperature. Figures 15-18 show examples of the SLC fracture morphology for 22 and $140^{\circ}C$. The SLC fracture morphology is primarily ductile rupture with accompanying tear ridges in contrast to the quasi-cleavage exhibited by the fatigue fracture surfaces. Figure 19 shows the extent of crack tunneling for the -30, 22 and $140^{\circ}C$ temperatures at the 65 $MPa\sqrt{m}$ starting $K_{\max}$ level; crack tunneling significantly increase as the temperature drops. Figure 20 is a plot of average and maximum tunneling crack depths as a function of reciprocol temperature for starting $K_{\max}$ values of 60 and 65 $MPa\sqrt{m}$. The straight-line behavior exhibited by the data suggests that the crack tunneling is thermally-activated. Data points for room temperature 60 $MPa\sqrt{m}$ tests with a 0.2% superposed ripple-load ($0.12 MPa\sqrt{m}$) at 25 and 50 *Hz* are included and show a slightly larger degree of tunneling.

Conclusions and Recommendations

High stress-ratio fatigue and sustained-load cracking experiments were performed to characterize the crack growth behavior of a Ti-6Al-4V forging material in the duplex-annealed condition. The experimental results show that:

1. The $R = 0.9$ fatigue crack growth data show no temperature effects in the 22 to $140^{\circ}C$ range; classical power-law growth in the intermediate ΔK regime; an overall threshold value of: $\Delta K_{th} \approx 2.04 MPa\sqrt{m}$; and a fracture morphology consisting of blocky cleavage and secondary cracking.

2. The $K_{\max}$ constant-decreasing ΔK fatigue crack growth data show no temperature effects in the 22 to $140^{\circ}C$ range; an overall threshold value of: $\Delta K_{th} \approx 2.00 MPa\sqrt{m}$; and a fracture morphology consisting of both cleavage and ductile rupture features.

3. The constant-load tests, with *K* levels near the fracture toughness, exhibited transient crack growth; crack tunneling depths that increase with decreasing temperature and follow an Arrhenius-like temperature dependence; and a ductile rupture morphology.

The transient nature of the SLC, and the large plastic deformation occurring at the specimen sides during SLC suggest the need for experiments on thicker or side-grooved specimens. This would increase the degree of plane strain experienced by the crack thereby increasing the susceptibility to SLC. Assuming steady-state SLC is observed, additional fatigue and SLC tests to assess the effects of *K*, temperature and internal hydrogen would be required to develop a more robust damage tolerant design methodology for gas-turbine components.

Acknowledgments

Partial financial support of this project by AFOSR and Wright Laboratory under RDL Grant #97-0810 and supply of the Ti-6Al-4V plate forging material by Dr. T. Nicholas at Wright Laboratory are gratefully acknowledged.

References

1. T. Nicholas and J.R. Zuiker, *Int. J. Frac.*, 80, 219, (1996).

2. B.A. Cowles, *Int. J. Frac.*, 80, 147, (1996).

3. High Cycle Fatigue Science and Technology Program Annual Report, AFRL-PR-WP-TM-1998-2002, (1998).

4. H.W. Rosenberg, J.C. Chesnutt, and H. Margolin, in *Application of Fracture Mechanics for Selection of Metallic Structural Materials*, American Society for Metals, OH, 213, (1982).

5. J.C. Chesnutt, A.W. Thompson, and J.C. Williams, "Influence of Metallurgical Factors on the Fatigue Crack Growth Rate in Alpha-Beta Titanium Aloys", AFML-TR-78-68, Rockwell International, CA, (1978).

6. D.N. Williams, *Matls. Sci. & Engr.*, 24, 53, (1976).

7. R.R. Boyer and W.F. Spurr, *Met. Trans. A*, 9A, 23, (1978).

8. D.A. Meyn, *Met. Trans A*, 5A, 2405, (1974).

9. G.R. Yoder, C.A. Griffis, and T.W. Crooker, *ASME J. Engr. Mat's and Tech.*, Oct., 286, (1974).

10. W.H. Reimann, *J. Matls.*, JMLSA, 6, 926, (9171).

11. A.D. Freed and B.I. Sandor, in *Cavities and Cracks in Creep and Fatigue*, Applied Science, UK, 89, (1981).

12. D. Eylon, "Summary of the Available Information on the Processing of the Ti-6Al-4V HCF/LCF Program Plates", Wright Laboratory/WLLM Internal Report, (1998).

13. ASTM, Annual Book of Standards, Vol 03.01, American Society of Testing and Materials, PA, 557, (1997).

14. A. Yeun, S.W. Hopkins, G.R. Leverant, and C.A. Rau, Met. Trans. A, 5A, 1833, (1974).

15. G. Marci, Fatigue, 16, 409, (1994).

16. G. Marci, in Proceedings of the 6th Internatinal Fatigue Congress, Berlin, Germany, Vol. 1, 493, (1996).

17. M. Lang, G.A. Hartman, and J.M. Larsen, Scripta Materialia, 38, 1803, (1998).

References

1. T. Nicholas and J. R. Zuiker, *Int. J. Frac.*, 80, 219, (1996).
2. B. A. Cowles, *Int. J. Frac.*, 80, 147, (1996).
3. High Cycle Fatigue Science and Technology Program Annual Report, AFRL-PR-WP-TM-1998-2002, (1998).
4. H. W. Rosenberg, J. C. Chesnutt, and H. Margolin, in *Application of Fracture Mechanics for Selection of Metallic Structural Materials*, American Society for Metals, OH, 213, (1982).
5. J. C. Chesnutt, A. W. Thompson, and J. C. Williams, "Influence of Metallurgical Factors on the Fatigue Crack Growth Rate in Alpha-Beta Titanium Alloys", AFML-TR-78-68, Rockwell International, CA, (1978).
6. D. N. Williams, *Matls. Sci. & Engr.*, 24, 53, (1976).
7. R. R. Boyer and W. F. Spurr, *Met. Trans. A*, 9A, 23, (1978).
8. D. A. Meyn, *Met. Trans. A*, 5A, 2405, (1974).
9. G. R. Yoder, C. A. Griffis, and T. W. Crooker, *ASME J. Engr. Matl's and Tech.*, Oct., 286, (1974).
10. W. H. Reimann, *J. Matls.*, JMLSA, 6, 926, (1971).
11. A. D. Freed and B. I. Sandor, in *Cavities and Cracks in Creep and Fatigue*, Applied Science, UK, 89, (1981).
12. D. Eylon, "Summary of the Available Information on the Processing of the Ti-6Al-4V HCF/LCF Program Plates", Wright Laboratory/WLLM Internal Report, (1998).
13. ASTM, Annual Book of Standards, Vol 03.01, American Society of Testing and Materials, PA, 557, (1997).
14. A. Yuen, S. W. Hopkins, G. R. Leverant, and C. A. Rau, Met. Trans. A, 5A, 1833, (1974).

15. G. Marci, Fatigue, 16, 409, (1994).
16. G. Marci, in Proceedings of the 6th International Fatigue Congress, Berlin, Germany, Vol. 1, 493, (1996).
17. M. Lang, G. A. Hartman, and J. M. Larsen, Scripta Materialia, 38, 1803, (1998).

TABLES

Table 1: Ti-6Al-4V Material Chemistry (Wgt. % [12])

Al	V	O	Fe	N	H^*
6.30	4.17	0.185	0.19	0.013	0.0051 ± 0.0003

*: $\pm$ 1 standard deviation.

Table 2: Longitudinal properties [12]

S_y (*MPa*)	S_u (*MPa*)	Elongation (%)	*E* (*GPa*)	Strain Rate (s^{-1})
930	979	20.1	120	5×10^{-4}
1003	1014	18.3	126.5	5×10^{-2}

FIGURES

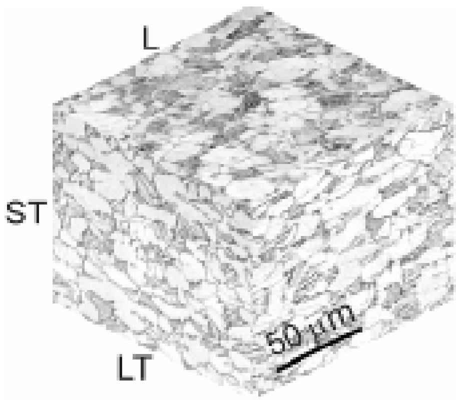

Figure 1: The microstructure for the duplex-annealed Ti-6Al-4V test material with α (light) and Widmanstätten $\alpha + \beta$ (dark) grains (Kroll's reagent; 15 *sec*). Slight flattening of the grains in the thickness direction is evident in the transverse planes.

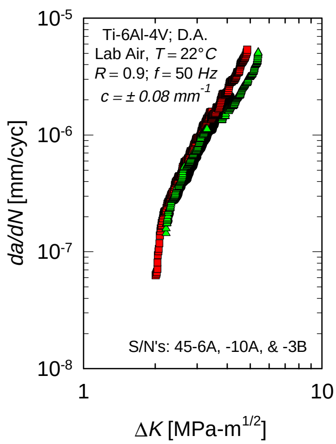

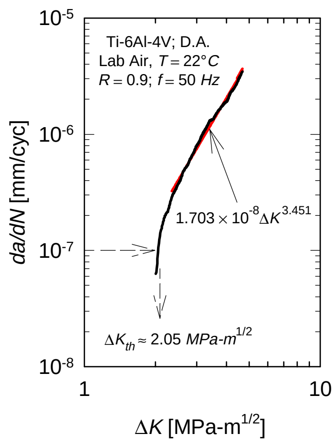

Figures 2a and b: Fatigue data for *R = 0.9* at $22^{\circ}C$; (a) scatter plot; (b) average.

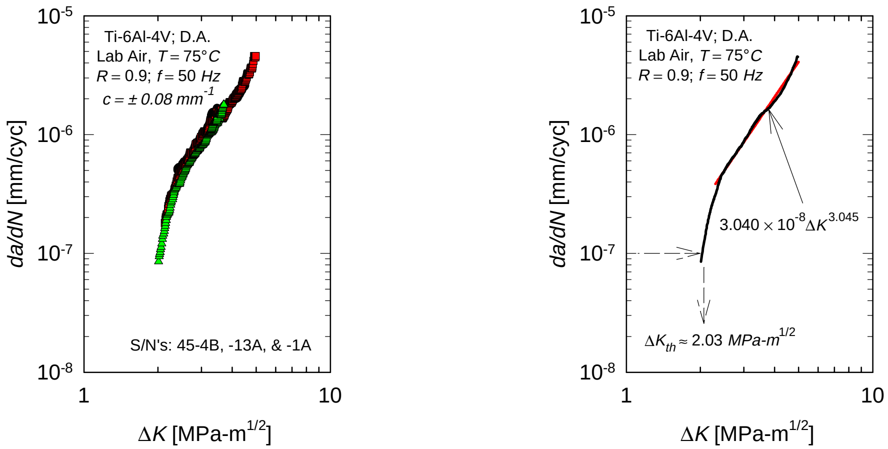

Figures 3a and 3b: Fatigue data for $R = 0.9$ at $75^{\circ}C$; (a) scatter plot; (b) average.

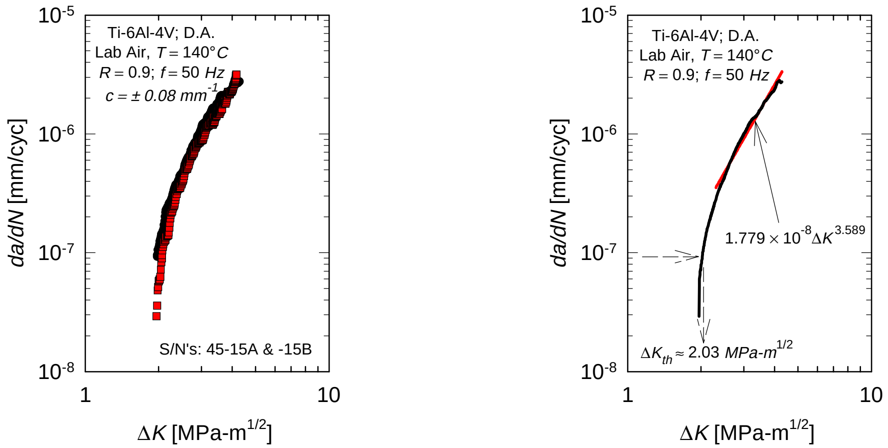

Figures 4a and 4b: Fatigue data for $R = 0.9$ at $140^{\circ}C$; (a) scatter plot; (b) average.

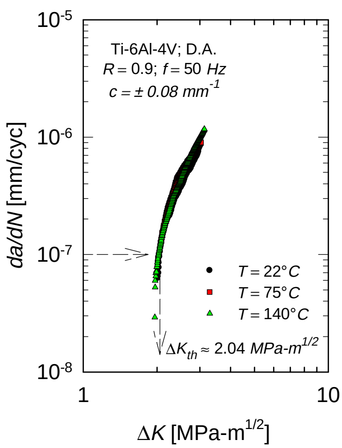

Figure 5: Fatigue data for R =constant at the various test temperatures.

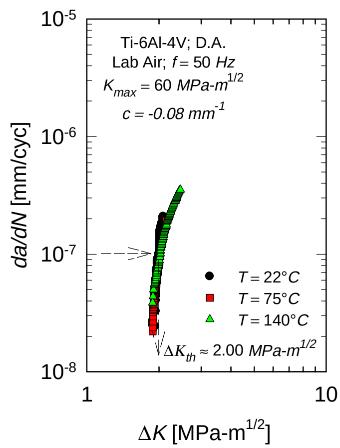

Figure 6: Fatigue data for $K_{\max}$ = constant at the various test temperatures.

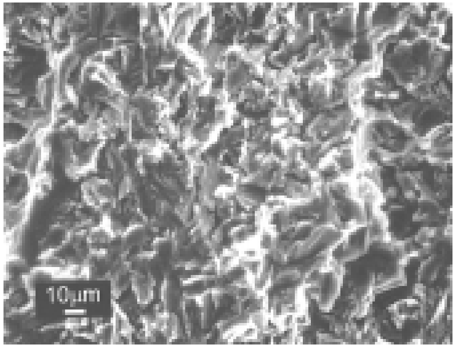

Figure 7: Fracture morphology for fatigue at ΔK_{th} and $22^{\circ}C$.

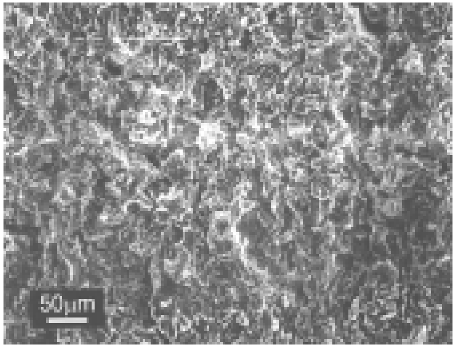

Figure 8: Transition from fatigue at ΔK_{th} (lower half) to power-law fatigue (upper half) at $22^{\circ}C$.

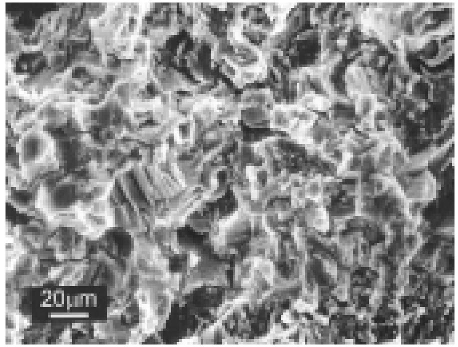

Figure 9: Fracture morphology for fatigue in the power-law regime at $22^{\circ}C$.

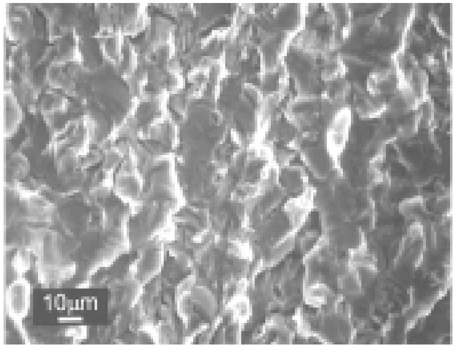

Figure 10: Fracture morphology for fatigue at ΔK_{th} and $140^{\circ}C$.

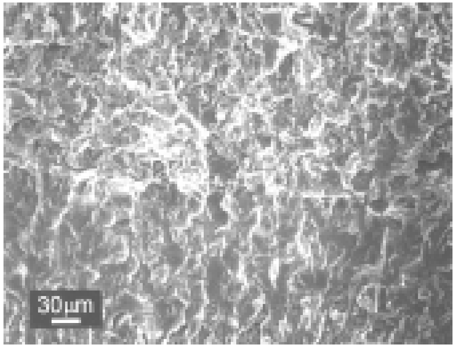

Figure 11: Transition from fatigue at ΔK_{th} (lower half) to power-law fatigue (upper half) at $140^{\circ}C$.

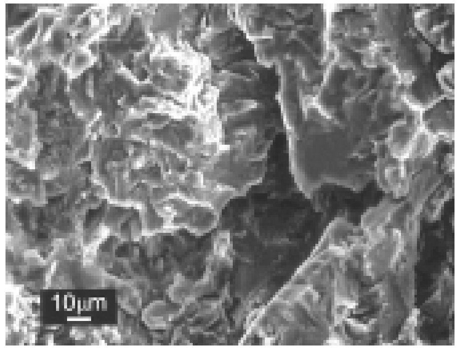

Figure 12: Fracture morphology for fatigue in the power-law regime at $140^{\circ}C$.

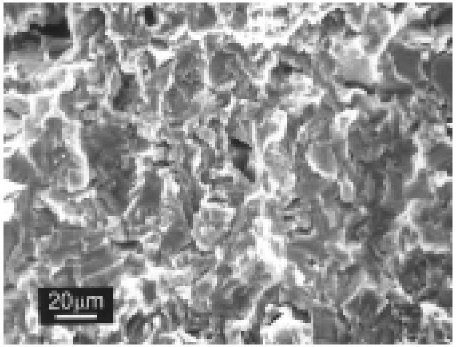

Figure 13: Fracture morphology for $K_{\max} = 60 MPa\sqrt{m}$ fatigue CG at $22^\circ C$.

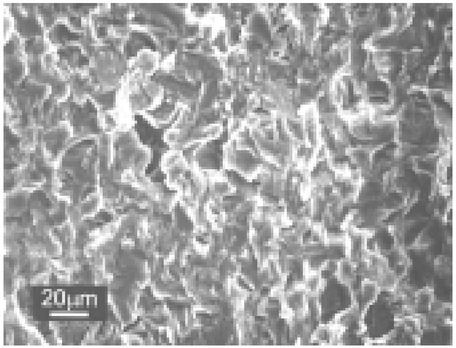

Figure 14: Fracture morphology for $K_{\max} = 60 MPa\sqrt{m}$ fatigue CG at $22^\circ C$.

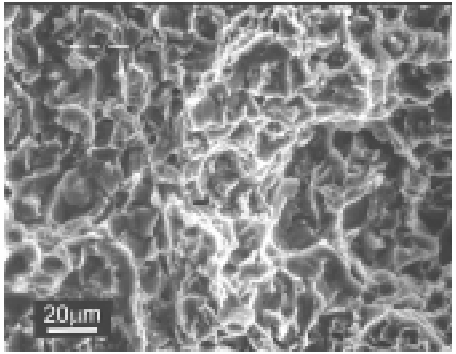

Figure 15: Fracture morphology for SLC with $K \approx 68 MPa\sqrt{m}$ and $22^\circ C$.

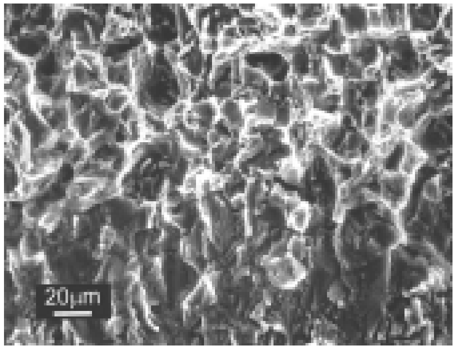

Figure 16: Transition from fatigue precracking (lower half) to SLC with $K \approx 68 MPa\sqrt{m}$ and $22^\circ C$.

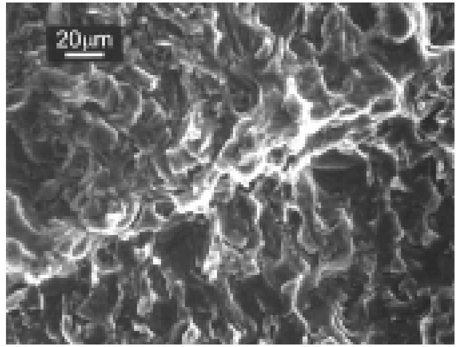

Figure 17: Fracture morphology for SLC with $K \approx 68 MPa\sqrt{m}$ and $140^\circ C$.

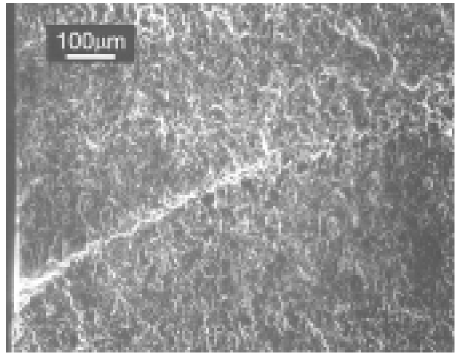

Figure 18: Transition from fatigue precracking (lower half) to SLC with $K \approx 68 MPa\sqrt{m}$ and $140^\circ C$.

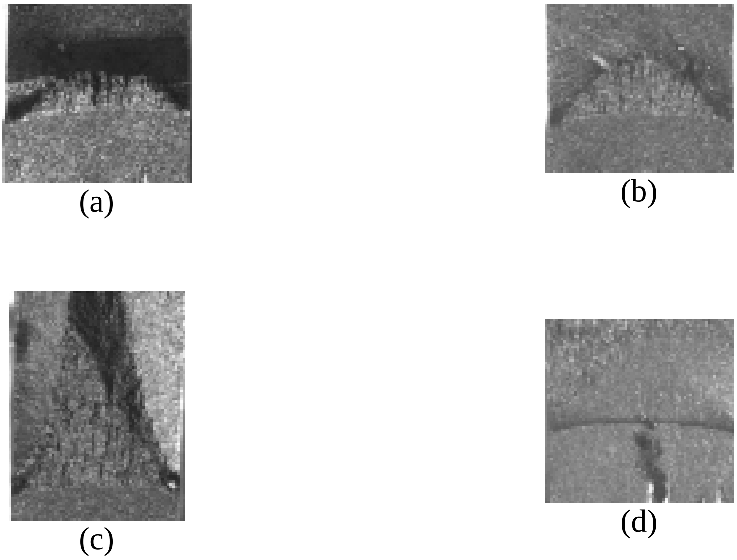

Figure 19: Final SLC shapes at various starting K levels and temperatures: (a) $K_i = 65MPa\sqrt{m}$ and $T = 22^\circ C$; (b) $K_i = 67.5MPa\sqrt{m}$ and $T = 22^\circ C$; (c) $K_i = 65MPa\sqrt{m}$ and $T = -30^\circ C$; and (d) $K_i = 65MPa\sqrt{m}$ and $T = 140^\circ C$.

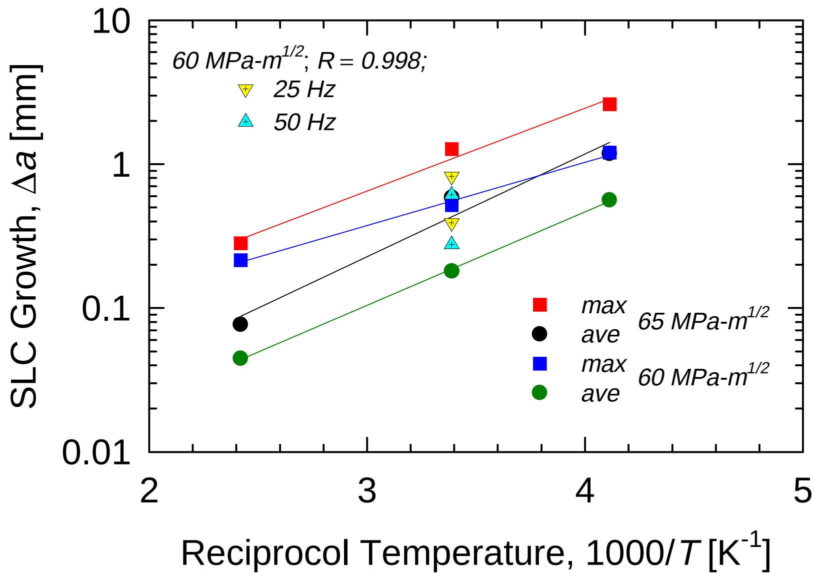

Figure 20: Arrhenius plot of the SLC growth for the maximum extent of the tunneled crack and the average tunneled crack length. Data points for SLC growth with a small ripple (~0.2% of K) load superimposed are also shown.

FOURIER ANALYSIS OF FRACTURE SURFACE TOPOGRAPHY TO DEDUCE FATIGUE LOAD SPECTRA

Takao Kobayashi, Ph.D. and Donald A. Shockey, Ph.D.
SRI International
333 Ravenswood Avenue
Menlo Park, CA 94025-3493

Advanced fracture surface analysis techniques were applied to titanium alloy specimens fractured in the laboratory under different HCF load conditions to determine whether load parameter changes produce quantifiable changes in the topography of the fracture surfaces. The goal was to identify a simple and objective signature of the fracture surface topography that relates to the load conditions that caused the fracture.

Round bar, compact tension (Figure 1), and surface flaw specimens were examined fractographically and elevation maps of the fracture surfaces (Figure 2) were produced by confocal optics microscopy. Fast Fourier transform (FFT) algorithms were applied to the topography data and elevation power spectrum density (EPSD) curves were obtained (Figure 3).

Under certain conditions, namely in load shedding experiments conducted at stress ranges ΔK above 8 ksi$\sqrt{m}$, the resulting EPSD curves discriminated between surfaces produced at different stress ranges. Furthermore, the ESPD curves obtained for surfaces produced under similar ΔK conditions distinguished those surfaces produced at different stress ratios. However, for other load spectrum conditions, for example at low ΔK ranges, the FFT analysis did not discriminate clearly among the failure surfaces. Nevertheless, these results are evidence that load spectrum information is encrypted in the deformation structure of fatigue failure surfaces.

We are currently seeking ways to relate the Fourier results to the load parameters to enable details of a spectrum load to be deduced from fracture

This material is based upon work supported by the US Air Force Research Laboratory under Contract No. F33615-96-C-5269.

surface topography. To estimate the load conditions responsible for in-service cracking of a specific aircraft engine component (Figure 4), we used empirical correlations and assumed relationships between surface roughness, process zone size, plastic zone size, and stress intensity to convert Fourier parameters to stress intensity range (Figures 5-7).

The fracture surface topography analysis suggested the crack in the failed engine component occurred under vibratory bending and provided a quantitative assessment of the stress intensity range as a function of crack length (Figure 8).

This material is based upon work supported by the US Air Force Research Laboratory under Contract No. F33615-96-C-5269.

Figure 1. Compact tension specimen in which HCF parameters were changed as the crack propagated, resulting in areas of fracture surface produced under different load conditions.

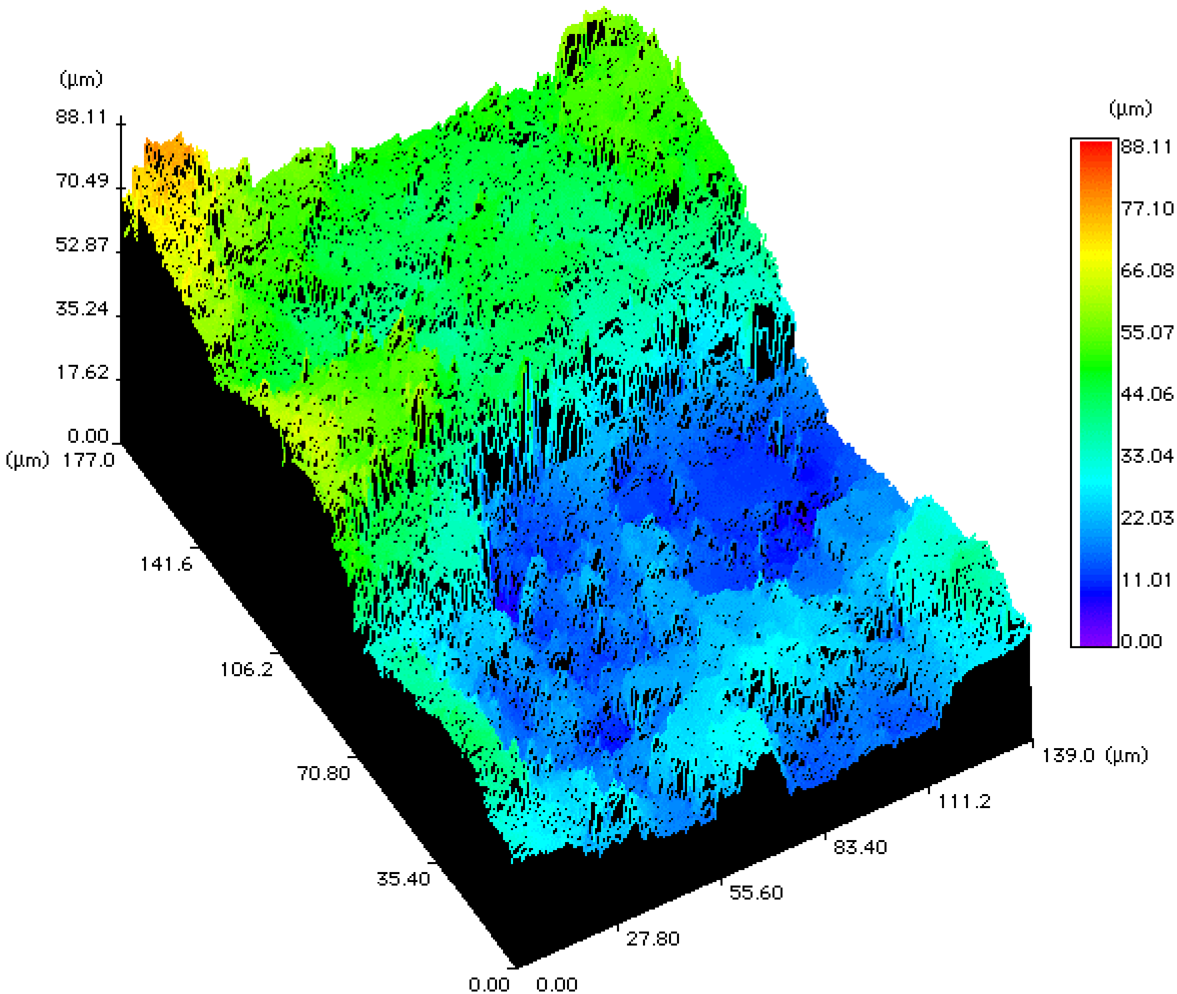

Figure 2. Isometric view of fracture surface topography obtained with a confocal optics scanning laser microscope.

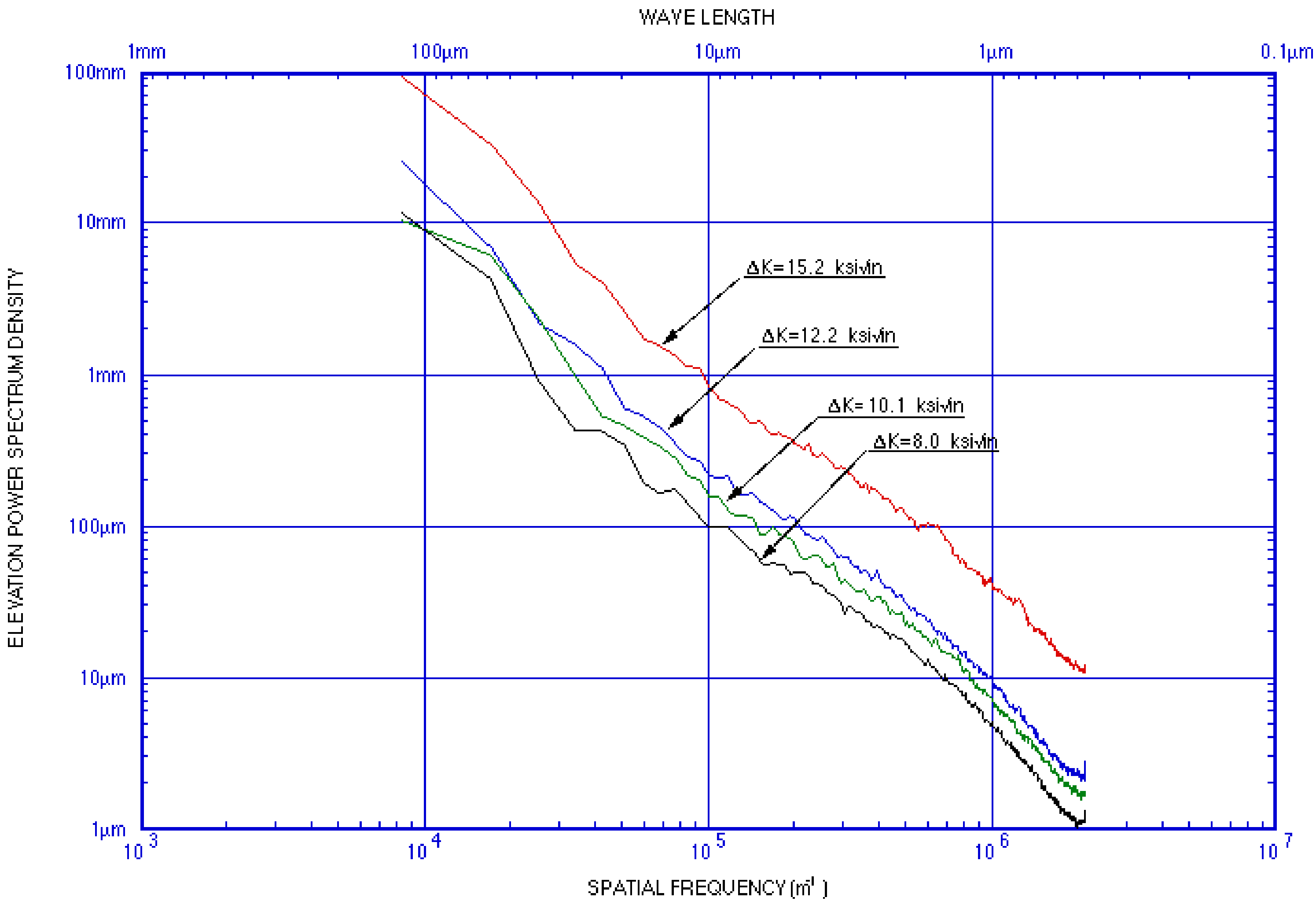

Figure 3. Fast Fourier transform results from fracture surface areas produced under different stress intensity ranges.

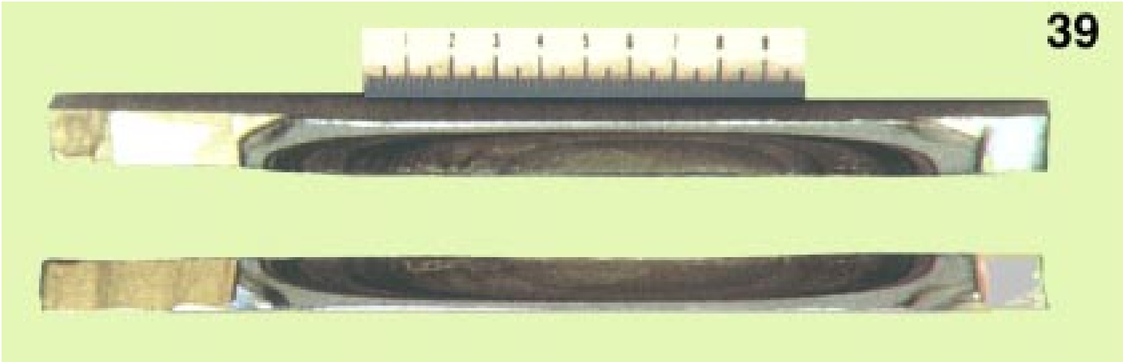

Figure 4. Fracture surfaces from a failed aircraft engine component.

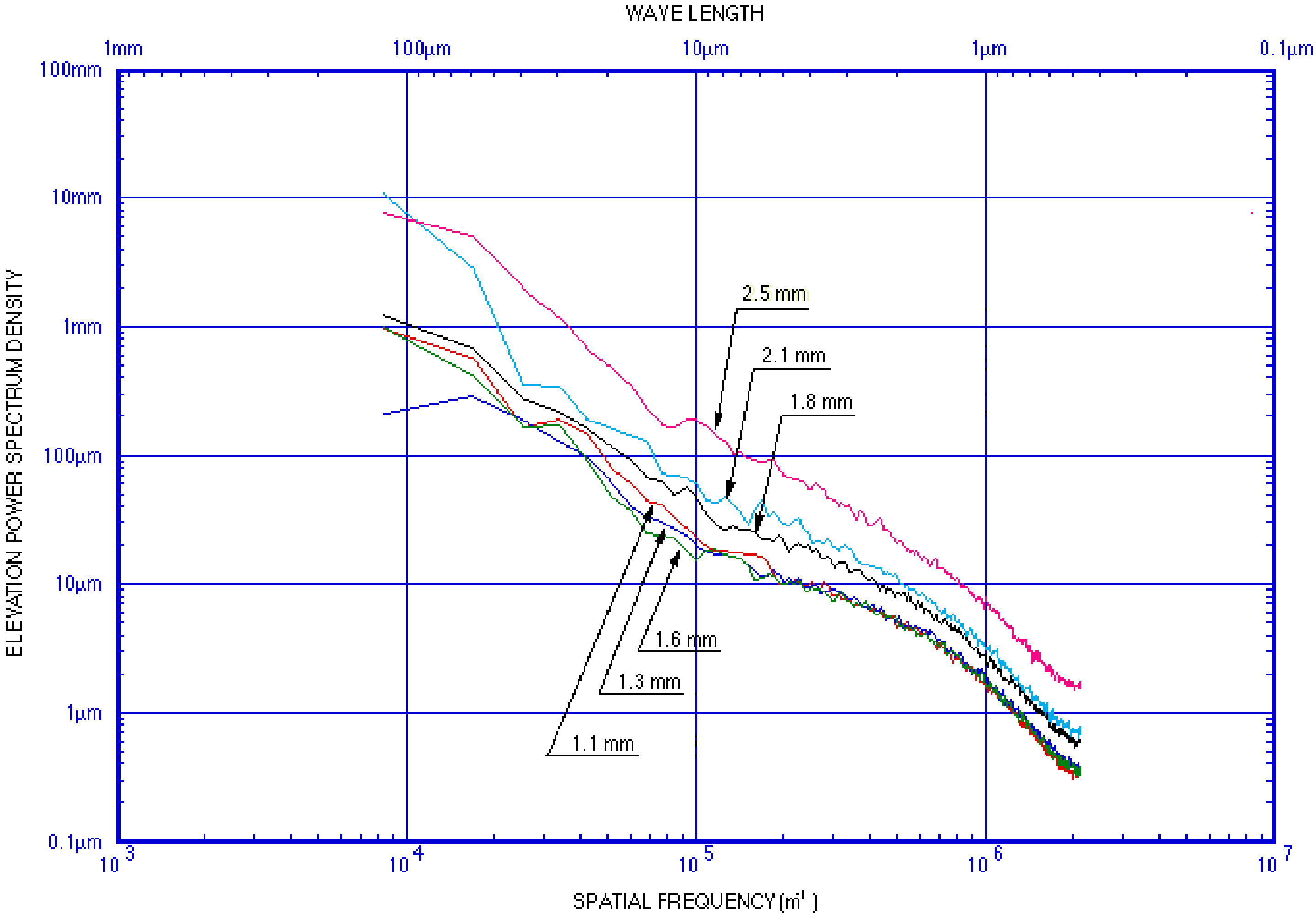

Figure 5. Elevation power spectrum density (EPSD) curves obtained from the component as a function of distance from the crack origin.

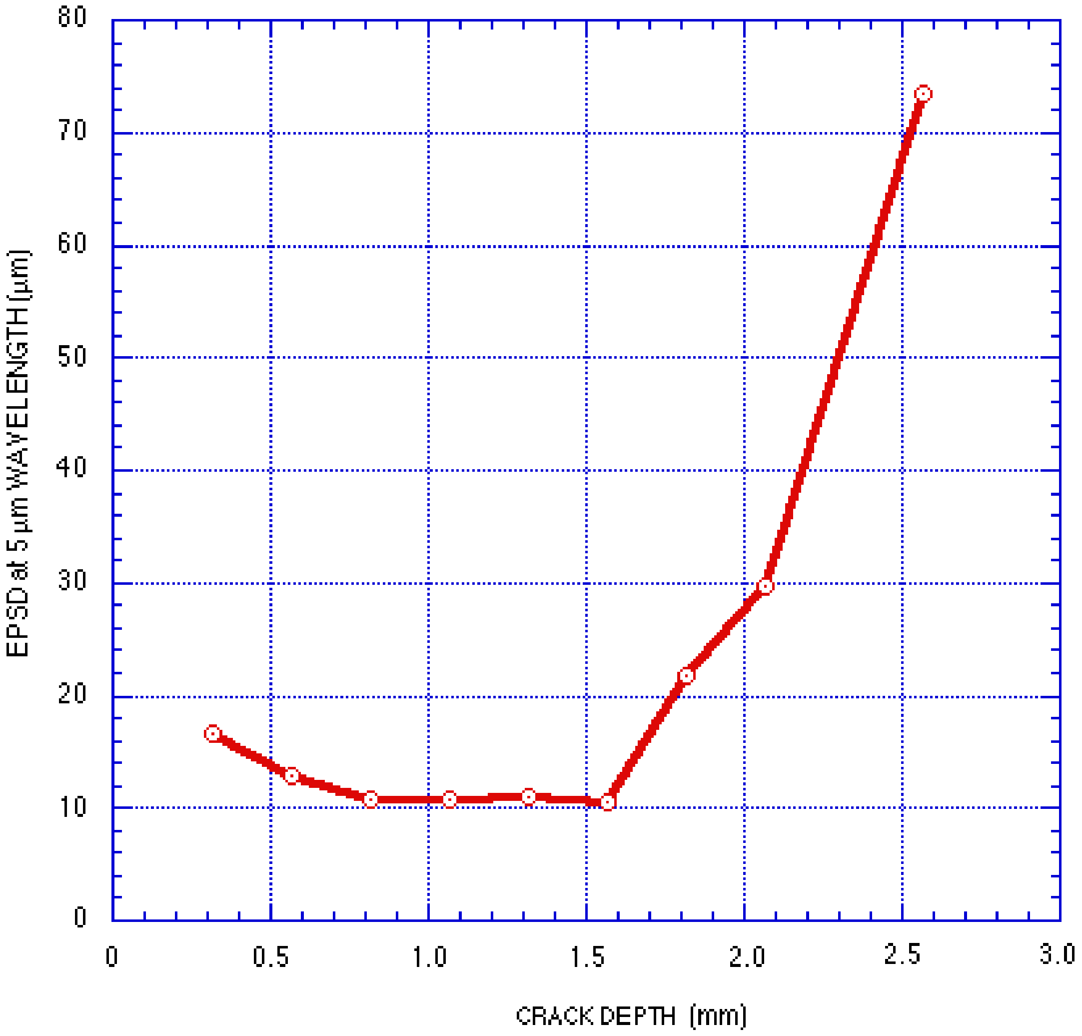

Figure 6. EPSD value at 5 micron wavelength versus crack depth.

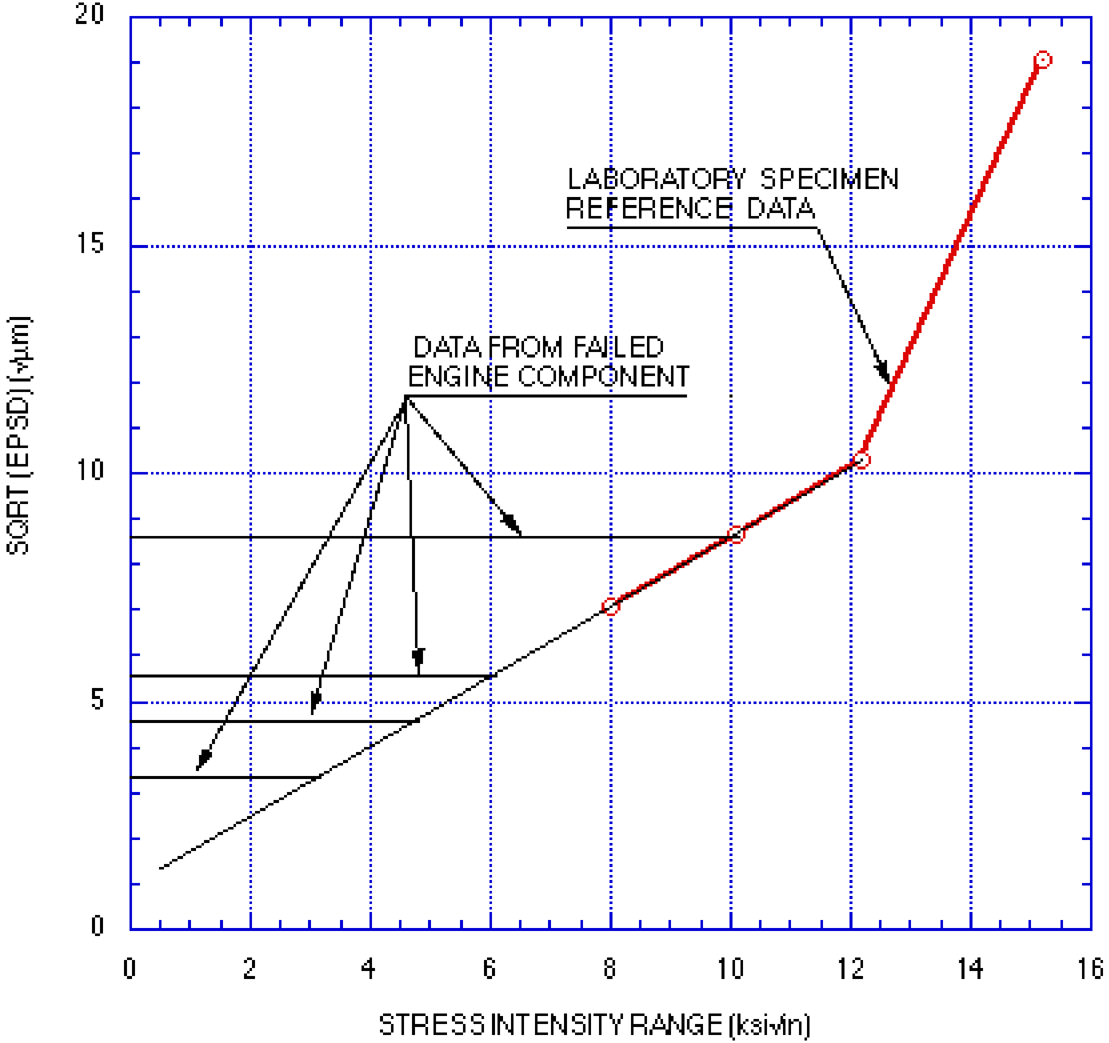

Figure 7. Correlation between $(EPSD)^{1/2}$ and ? K for the laboratory specimen and the engine component.

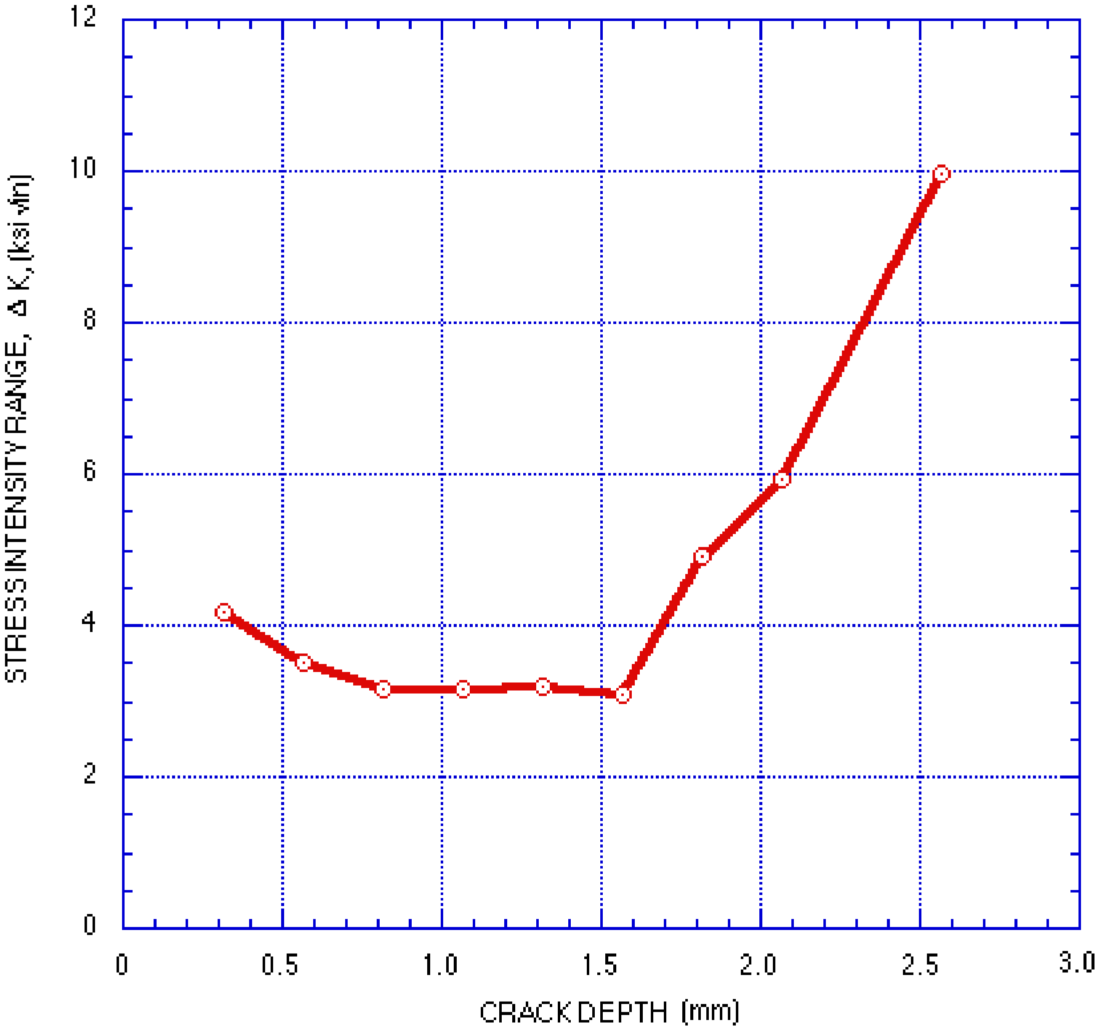

Figure 8. Quantitative estimate of ? K along the crack path for the failed engine component.